Flow morphology and heat transfer analysis during high-pressure steam condensation in an inclined tube part I: Experimental investigations

Bieberle, A.; Moonesi Shabestary, A.; Geißler, T.; Boden, S.; Beyer, M.; Hampel, U.;

Originally published:

February 2020

Nuclear Engineering and Design 361(2020), 110553

DOI: https://doi.org/10.1016/j.nucengdes.2020.110553

Flow morphology and heat transfer analysis during high-pressure steam condensation in an inclined tube part I: Experimental investigations

André Bieberle[1], Amirhosein Moonesi Shabestary[1,2], Thomas Geissler[2], Stephan Boden[2], Matthias Beyer[1], Uwe Hampel[1,2]

[1] Helmholtz-Zentrum Dresden - Rossendorf, Institute of Fluid Dynamics,
Bautzner Landstr. 400, 01328 Dresden, Germany.

[2] Chair of Imaging Techniques in Energy and Process Engineering,
Technische Universität Dresden, 01062 Dresden, Germany.

Email: a.bieberle@hzdr.de

Abstract

In this paper, experimental investigations on the flow morphology and heat transfer in a single steam condenser tube are presented, which were performed at the thermal hydraulic test facility COSMEA (COndensation test rig for flow Morphology and hEAt transfer studies). This facility has been setup to study the interrelation of condensation heat transfer with two-phase flow in an isolated single condenser tube that is cooled by forced convection. Studies have been performed for elevated pressures up to 65 bar at saturation conditions and for inlet steam mass flow of up to 1 kg/s and different inlet steam qualities. The wall heat flux is measured with distributed heat flux probe and global condensation rates have been obtained from integral heat and mass balances. As a unique feature the cross-sectional phase distribution has been studied via X-ray computed tomography. The data is going to be used for the validation of numerical simulations with 1D ATHLET and 3D CFD codes as presented in the second part of this paper.

Key words: condensation heat transfer, heat exchangers, two-phase flow, heat flux, X-ray tomography, passive safety systems

Nomenclature

A	Inner cross-sectional area [m²]	$\dot{m}$	Mass flux [kg/s]
b	Length of the flume cross-section arc	N	Number of pixels
C	Contrast [-]	$\dot{q}$	Heat flux [W/m²]
d	Diameter [m]	Q	Transferred heat [J]
g	Gravitational acceleration [m/s²]	r	Radius [m]
h	Heat transfer [W/m²/K]	Re	Reynolds number
H	Enthalpy [kJ/kg]	t	Time [s]
H'	Enthalpy of saturated water [kJ/kg]	T	Temperature [°C]
H''	Enthalpy of saturated steam [kJ/kg]	u	Velocity [m/s]
j	Superficial velocity [m/s]	$\dot{V}$	Volumetric flow rate [m³/h]
l	Length [m]	w	Weight function [-]
L	Level height (condensate) [m]	x	Steam mass fraction [-]

Subscripts

1	Large part of the separator vessel	ins	Thermal insulation
2	Small part of the separator vessel	l	Liquid
c	Condensate	o	Outer, outlet
cw	Cooling water	p	Primary side, partially
cy	Cylindrical part of the separator	r	flume
exp	Experiment	s	Steam
fw	Feed into the cooling water loop	sep	Separator vessel
g	Gas	th	Torospherical head of the separator
hl	Heat loss	w	Wall
Hu	Heat-up	x	Coordinate
hy	Hydraulic	y	Coordinate
i	Inner, inlet		

Greek symbols

α	Liquid fraction [-]	ν	Kinematic viscosity
δ	Wall thickness [m]	λ	Thermal conductivity [W/(mK)]
ε	Void fraction [-]	ρ	Density [kg/m³]
μ	Linear attenuation coefficient [1/m]		

Abbreviations

ATHLET	Analysis of THermal-hydraulics of LEaks and Transients
ATLAS	Advanced Thermal-Hydraulic Test Loop for Accident Simulation
APR	Advanced Power Reactor
CCC	Containment Cooling Condenser
CFD	Computational Fluid Dynamics
CFP	Core Flooding Pool
COSMEA	Condensation test rig for flow morphology and heat transfer study
CS	Cross-Section
CT	Computed Tomography
EC	Emergency Condenser
FI	Mass Flow Indication
GENEVA	GENEric investigations on passive heat remoVAl systems
HFP	Heat Flux Probe
HUSTLE	Hitachi Utility Steam Test Leading facility
INKA	INtegral Test Facility KArlstein
INVEP	Invert Edward Pipe
KAERI	Korea Atomic Energy Research Institute
KONWAR	Ger.: KONdensation in WAagerechten Rohren (condensation inside horizontal tubes)

NOKO	Ger.: NOtKOndensator (emergency condenser)
LI	Liquid Level Indication
LOCA	Loss Of Coolant Accident
MTF	Modulation Transfer Function
OPC	Open Platform Communications
PAFS	Passive Auxiliary Feedwater System
PASCAL	PAFS Condensing Heat Removal Assessment Loop
PI	Pressure Indication
PPPT	Passive Pressure Pulse Transmitter
RPV	Reactor Pressure Vessel
SCL	Stratified Condensate Level
SWR	Ger.: Siedewasser-Reaktor (Boiling Water Reactor)
SETCOM	Separate Effect Test for COndensation Modeling
TDI	Temperature Difference Indication
TE	Ger.: Thermoelement (Thermocouple)
TI	Temperature Indication
TOMO	Tomographic imaging plane
TOPFLOW	Transient twO Phase FLOW test facility

1. Introduction

Today, safety systems in nuclear power plants do mostly rely on active components. For the removal of decay heat after a reactor shutdown, for instance, coolant circulation in the primary circuit is sustained via pumps. This is, however, a potential safety risk in case of a station black-out as it was experienced in 2011 at the Fukushima Daiichi Nuclear Power Plant. Therefore, future nuclear power plant designs shall utilize passive safety systems which are independent from electrical power [1]-[7]. One of these improved reactor concepts is the boiling water reactor KERENA^{TM} that combines a new passive safety control strategy with the advantages of a Generation III+ nuclear reactor design [2] (see Figure 1). Besides being a very economic design due to its simple operational concept and configuration it comprises several passive safety systems such as a passive pressure pulse transmitter for thermal-hydraulic actuation, core-flooding lines, drywell flooding lines, pressure suppression and venting systems for pressure reduction and hydrogen blow off, and a fully passive heat removal chain including an emergency condenser and a containment cooling condenser for transferring heat from the reactor pressure vessel to the storage pool outside the containment. Additionally, large water volumes are provided, such as a core flooding pool (CFP), a pressure suppression pool and a storage pool actuating as passive heat sink for maximal three days.

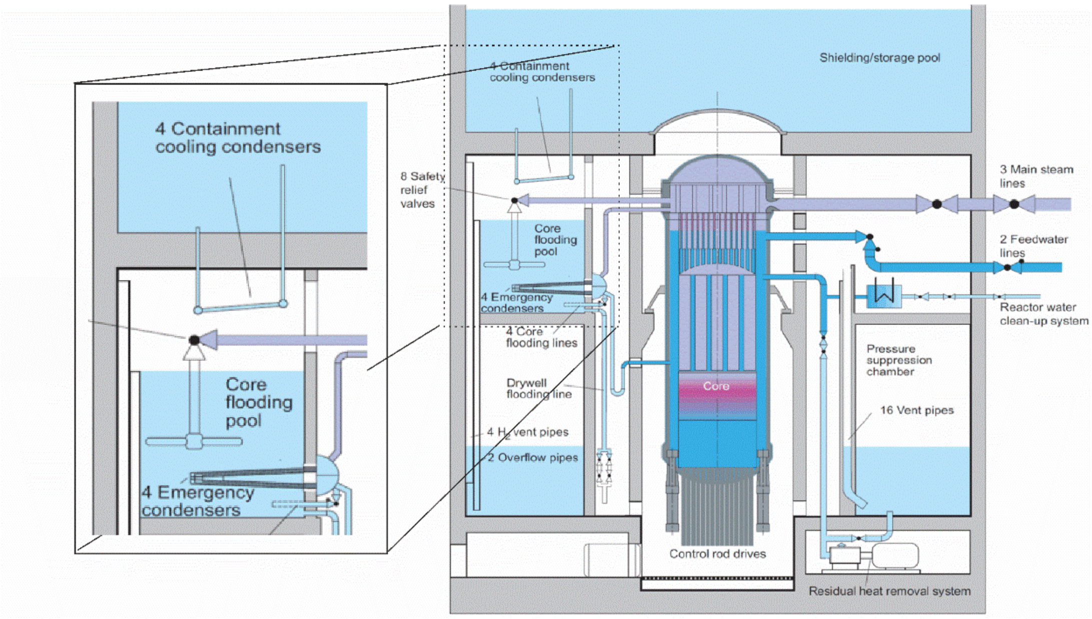

Figure 1: KERENA^{TM} reactor concept with passive safety systems (Stosic et al, 2008) [2].

The basic design and function of the KERENA heat removal chain is illustrated in Figure 1. There are four emergency condensers (EC) which are hydraulically connected to the reactor pressure vessel (RPV) via a steam line (top) and a condensate return line (bottom). Note, that Figure 1 shows only one of four ECs. Each EC is located inside the core flooding pool and is made of 61 lying U-shaped condenser tubes [8]. As the EC is directly connected with the RPV it is filled with the primary circuit water during reactor operation. As there is no circulation in this circuit the water temperature is close to that of the CFP.

In a loss of coolant accident (LOCA), such as a break of a main steam line or any other leakage, the resulting pressure loss leads to steam production in the primary circuit. The steam accumulates at the top of the RPV and the liquid filling level in the RPV and the connected circuit decreases. At some point high pressure steam enters the ECs and is there condensed. This starts a circulation in the EC loops, which is driven by steam production in the RPV and the steam condensation in the EC. Thus, a passive heat removal circuit is sustained. After some time the water in the CFP becomes saturated and starts boiling. At that moment four so-called containment cooling condensers (CCCs) above the core flooding pool start their action and transfer heat across the containment barrier. They are connected at their secondary side to the storage pool, whose water is at room temperature at the beginning of the CFP cooling and remains below 100 °C during emergency cooling. The subcooled liquid of the storage pool enters the CCCs while steam rising from the flooding pool is condensed on the outside of the CCC tubes. Hence, the water in the CCC evaporates and this drives another passive heat transfer to the storage pool.

Nuclear safety assessments that involve thermal hydraulics are today carried out with system codes such as AC² ATHLET, RELAP, and TRACE. While these codes have been well qualified for active hydraulic circuits there is still a need to qualify them for passive decay heat removal systems. For that, experimental data is needed. In this paper we report on an experimental studies on the condensation process inside an inclined tube under operation condition of an emergency condensers. They have been carried out at the COSMEA (COndenSation test rig for flow Morphology and hEA transfer studies) which is part of the TOPFLOW facility at Helmholtz-Zentrum Dresden Rossendorf (HZDR). We studied global and local heat transfer as well as flow morphology for different pressures up to 65 bar and different inlet qualities.

2. Past experimental activities with respect to KERENA passive heat removal systems

In the recent past a number of experimental investigations have already been performed with respect to the local and integral behaviour of the KERENA passive cooling circuit components. They will be briefly discussed in the following. The INtegral test facility KArlstein (INKA) at Framatome GmbH [9] was designed to experimentally investigate the passive safety systems of the KERENA reactor on an integral scale (see Figure 2). Amongst others the facility comprises large vessels representing the

KERENA containment and the large water volumes of the storage pool, the core flooding pool and the pressure suppression chamber and one of the four heat removal systems (EC, CCC). The pressure vessel is designed for operating pressures up to 160 bar and a maximum power of 22 MW. The whole facility is equipped with more than 300 sensors for temperature, mass flow, absolute and differential pressure as well as two-phase distribution. INKA provides a 1:1 height and a 1:24 volumetric scaling. In INKA there is also a number of smaller KERENA components integrated for testing. These are the passive pressure pulse transmitter (PPPT), vent pipes and core flooding lines are modelled too. The PPPT is a passive switching device that is used to directly initiate reactor shut down, containment isolation at the main steam line penetrations and automatic depressurization of the reactor pressure vessel (RPV). The vent pipes are designed for limiting the pressure increase in the containment to maximal 4 bar by steam release to and condensation in the pressure suppression chamber. The core flooding lines are used to inject additional cooling water from the CFP into the RPV by means of gravity flow at low-pressure condition. The more interested reader may be referred to [9]**.**

The INKA facility is used to assess the integral and component behaviour for different accident scenarios, such as steam-line breaks, RPV bottom leaks, or station black-out. From the extensive instrumentation it is possible to extract some information on single effects, such as steam flow and condensate level in EC single tubes, influence of non-condensable gases on the heat transfer inside the EC, two-phase instabilities in the CCC, as well as effects of natural convection on temperature stratification and gas composition in vessels. However, for a very detailed thermal hydraulic analysis that involves local flow and heat transfer conditions the instrumentation density is too low.

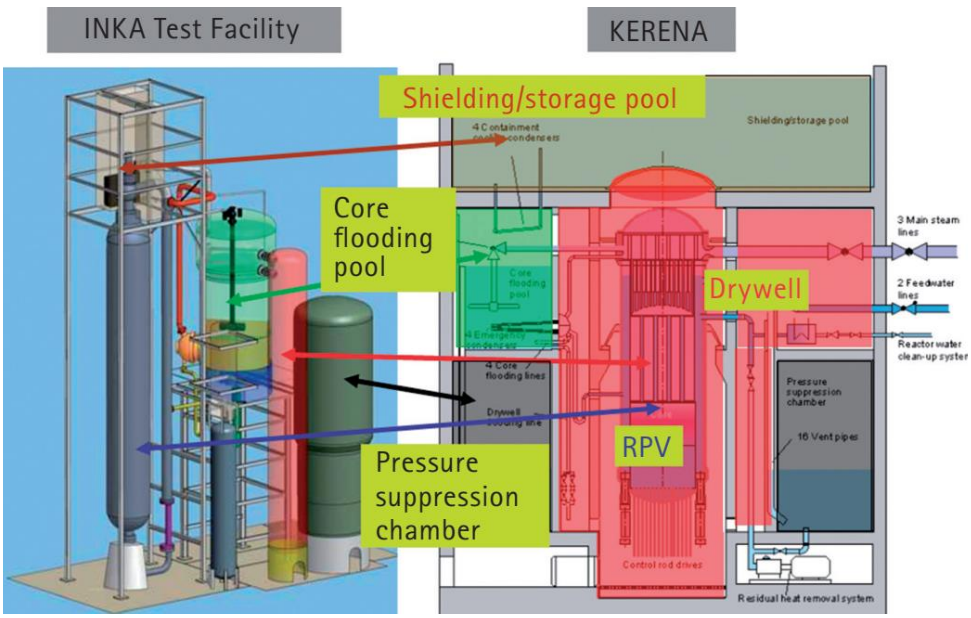

Figure 2 INKA test facility [9] regarding the KERENA reactor concept [2].

Single effect studies for the KERENA passive safety systems are being or were carried out at the facilities described in the following. The GENEVA test facility (GENEric investigations of passive heat remoVAl systems) is dedicated to single effect studies in the CCC [15]. It consists of four or fewer condenser tubes in a steam chamber which are connected to an upper reservoir with a height scaling equal to KERENA. The steam chamber emulates flooding pool conditions. Steam is fed into the chamber from a 120 kW evaporator via eight equally distributed nozzles and there slowed down by baffle plates. While the steam condenses at the condenser tubes, heat is being transferred to the inside where boiling sets in. The resulting density changes create a natural upward flow in the riser tube. In the downcomer tube sub-cooled liquid flows back into the condenser tubes what closes the natural circulation. Experiments are being carried out to investigate natural convection and flow instabilities, such as flashing and geysering, in detail. An upgrade of GENEVA was presented in 2017 by Viereckl et al. [16] applying advanced measurement technique such as multipoint level sensors for a better resolution of the two-phase flow structure inside the pipes as well as improved instrumentation to get axial and circumferential temperature profiles and condensation rates in the steam chamber. The whole experimental program is accompanied by system code analyses.

Until some years ago the so called NOKO facility (Ger.: NOtKOndensator) was operated at Forschungszentrum Jülich. It has been designed to investigate the effectiveness of the emergency condensers of the SWR 1000 reactor design [18], which is very similar to the KERENA one. Investigations were carried out for an eight tube EC bundle having original materials and geometry of the SWR 1000 design. The EC was submerged in a large tank and supplied with 10 MPa steam from an electro boiler. Intensive instrumentation with thermocouples and void probes allowed transient measurement of liquid distribution and condensation heat transfer on the primary side for different experimental scenarios, among them such with non-condensable gases. The emergency condenser power has been correlated to system pressure, condensation level and concentration of non-condensable gases. Based on the results, the numerical system code ATHLET was expanded by the so-called KONWAR heat transfer model, adding the ability to calculate condensation heat transfer in inclined tubes [19]. In 2001, the NOKO facility was dismantled and parts of it transferred to the TOPFLOW facility (Transient TwO Phase FLOW Test Facility) at Forschungszentrum Rossendorf (now Helmholtz-Zentrum Dresden-Rossendorf) [20]-[22]. At TOFLOW further studies on the role of secondary side boundary and flow conditions were carried out and accompanied by computational fluid dynamics (CFD) modelling for large vessels [23]-[29]. The level of detail on the primary side condensation obtained at NOKO and TOPFLOW was still rather low. Only information about axial temperature profiles could be obtained with multiple thermocouples and axial phase indicator distributions with multiple void probes. Therefore, we recently commissioned the thermal hydraulic test facility COSMEA at TOPFLOW to study the high-pressure steam condensation in a single inclined tube.

Eventually, we shall just briefly note that there are numerous other facilities in the context of nuclear safety research which address similar problems of condensation heat transfer. Among them are the LAOKOON facility for studying direct contact condensation on a sub-cooled water surface [30], the SETCOM facility for investigating the wall condensation and effects of inclination angle on heat transfer [31], the INVEP facility for investigation of condensation inside an inclined pipe which is immersed in a tank of sub-cooled water and for pressures of up to 10 bar [34]. As another example, KAERI (Korea Atomic Energy Research Institute) operates the ATLAS facility for thermal hydraulic analyses for the APR1400 reactor system. There, experiments on the Passive Auxiliary Feedwater System (PAFS) were performed in the PASCAL and ATLAS-PAFS test setups, which included studies on condensation heat transfer in a lying U-tube heat exchanger similar to the one in KERENA [35], [36].

3. Experimental setup and conditions

3.1 Experimental facility

Figure 3 shows a schematic representation of the COSMEA facility. It is essentially a single condenser tube with 43.1 mm inner diameter, 48.3 mm outer diameter, 2.6 mm wall thickness, 2992 mm length of heat transfer and a nominal inclination angle of 0.76 ±0.05° to the horizontal. Note, that the latter is only nominal as manufacturing tolerances and thermal expansion lead to slightly different inclinations values as given in section 3.5.4 and 4.1. The tube material is stainless steel type 1.4571. The test rig can be operated at up to 65 bar pressure and corresponding saturated steam temperatures. The condenser tube is coaxially jacketed by a cooling tube with an outer diameter of 120 mm and a wall thickness of 2.0 mm made of grade 2 titanium alloy. The cooling circuit is operated at max. 4 bar. The condenser tube is thus cooled via forced annular convective counter-current flow which provides well-defined cooling conditions. During operation of COSMEA the condenser tube is fed either with pure steam or a mixture of steam and saturated water via an in-house developed two-phase mixer described in detail in the next chapter. Both fluids are provided by the steam generator circuitry of the TOPFLOW facility. At the outlet of the condenser tube the two-phase mixture flows tangentially into a properly dimensioned separation vessel (inner diameter 550 mm) where the residual steam and the liquid are naturally separated. Both fluids are drained through separate tubes into the TOPFLOW blow-off tank.

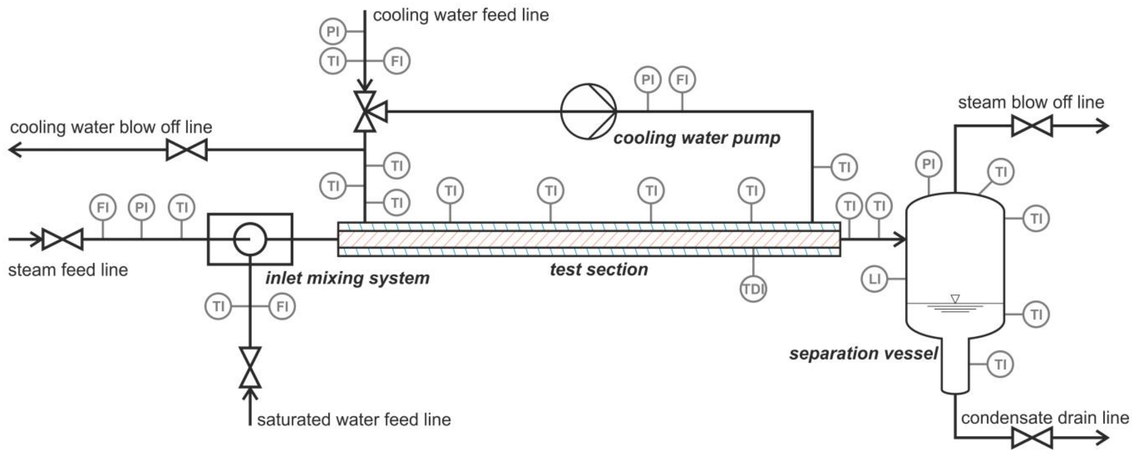

Figure 3: Scheme of the COSMEA facility (TI: temperature indication, PI: pressure indication, FI: mass flow indication, LI: liquid level indication, TDI: temperature difference indication).

The cooling water is circulated through the outer annulus with high mass flow. In this way, the heat-up is minimized to a few Kelvin which allows controlling the heat transfer via the flow rate. The temperature of the cooling water is controlled via the feed-and-split system shown in Figure 3. While the major part of the cooling water is re-circulated through the annulus by the cooling water pump, a minor part is extracted via the cooling water blow-off line and at the same time compensated by feed from the cooling water feed-line. This way, the circulation loop is always in liquid single-phase conditions. To achieve a high and homogenous heat flux, five swirl generators are installed along the annular gap as shown in Figure 4 and Figure 5 (bottom part). The first one is positioned directly after the cooling water inlet and the other ones in equal distances along the tube and near the temperature sensors.

The cooling water circulation loop is equipped with several temperature sensors. As shown in Figure 3 there is one thermocouple at the inlet, three at the outlet and four more at intermediate positions in equidistant places. Additionally, there are five thermocouples circumferentially distributed at an axial position 2052 mm downstream the inlet, which are used to detect inhomogeneous temperature distributions. Furthermore, there are absolute pressure sensors upstream the two-phase mixer and inside the separation vessel and differential pressure sensors across the two-phase mixer. All sensors were calibrated and their residual maximal measuring uncertainties determined as: temperature: ±0.3 K, pressure: ±1%, mass flow steam: ±2.2% and liquid mass flow: ±1.0%.

Two special measurement systems are additionally installed: a) an X-ray computed tomography (CT) scanner that provides time-averaged cross-sectional images of the local flow morphology and b) a heat flux probe (HFP) that allows a determination of the circumferential wall heat flux distribution at a given axial position. Detailed information about both systems is given in the next chapters. In Figure 5, the axial positions of the temperature sensors and special instrumentation are shown.

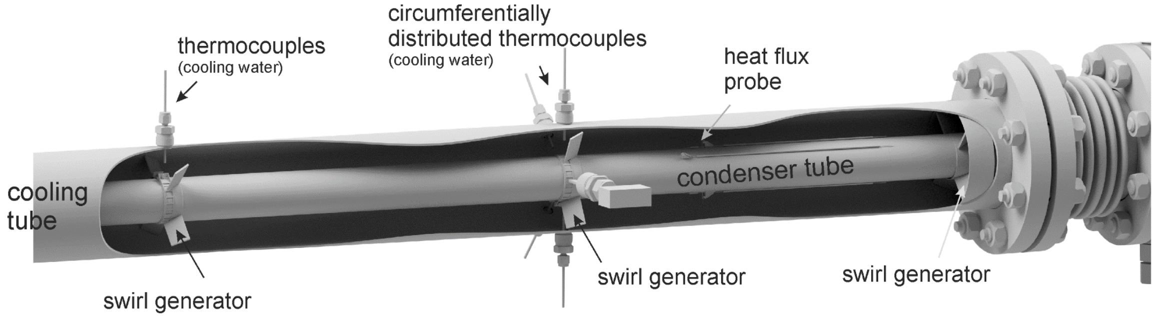

Figure 4: Cut-view of a part of the COSMEA facility discovering the swirl generators and instrumentation on the secondary (cooling) side.

The operational data of COSMEA are recorded by a programmable logic controller that allows raw data receipt, conversion and calibration as well as process control and process synchronization. The operational data are sampled with a frequency of 1 Hz on an OPC (Open Platform Communications) server. The HFP data are managed by a separate controller with a sampling frequency of 3 Hz. Also the data of the X-ray CT scanner is stored on a separate computer. The synchronization of all measurement systems is realized by a common trigger signal that is provided by the tomographic system. In Table 1 the range of experimental parameters as well as important geometric dimensions of the COSMEA facility are listed.

Table 1: Compiled experimental parameters for condensation experiments at the COSMEA facility.

Primary side parameters	
Pressure Temperature Steam mass flow (inlet) Water mass flow (inlet)	5 – 65 bar 152 – 281 °C 0.079 – 1.0 kg/s 0 – 0.751 kg/s
Cooling water parameters	
Pressure Water mass flow Temperature (mean)	3.0 - 4.0 bar 13 - 24 kg/s nominal 45.5 °C
Condenser tube parameters	
Material	stainless steel (1.4571)
Wall thickness	2.6 mm
Heat flux length	2992 mm
Inclination	nominal 0.76 ±0.05° measured 0.88 ±0.035°
Inner diameter	43.1 mm

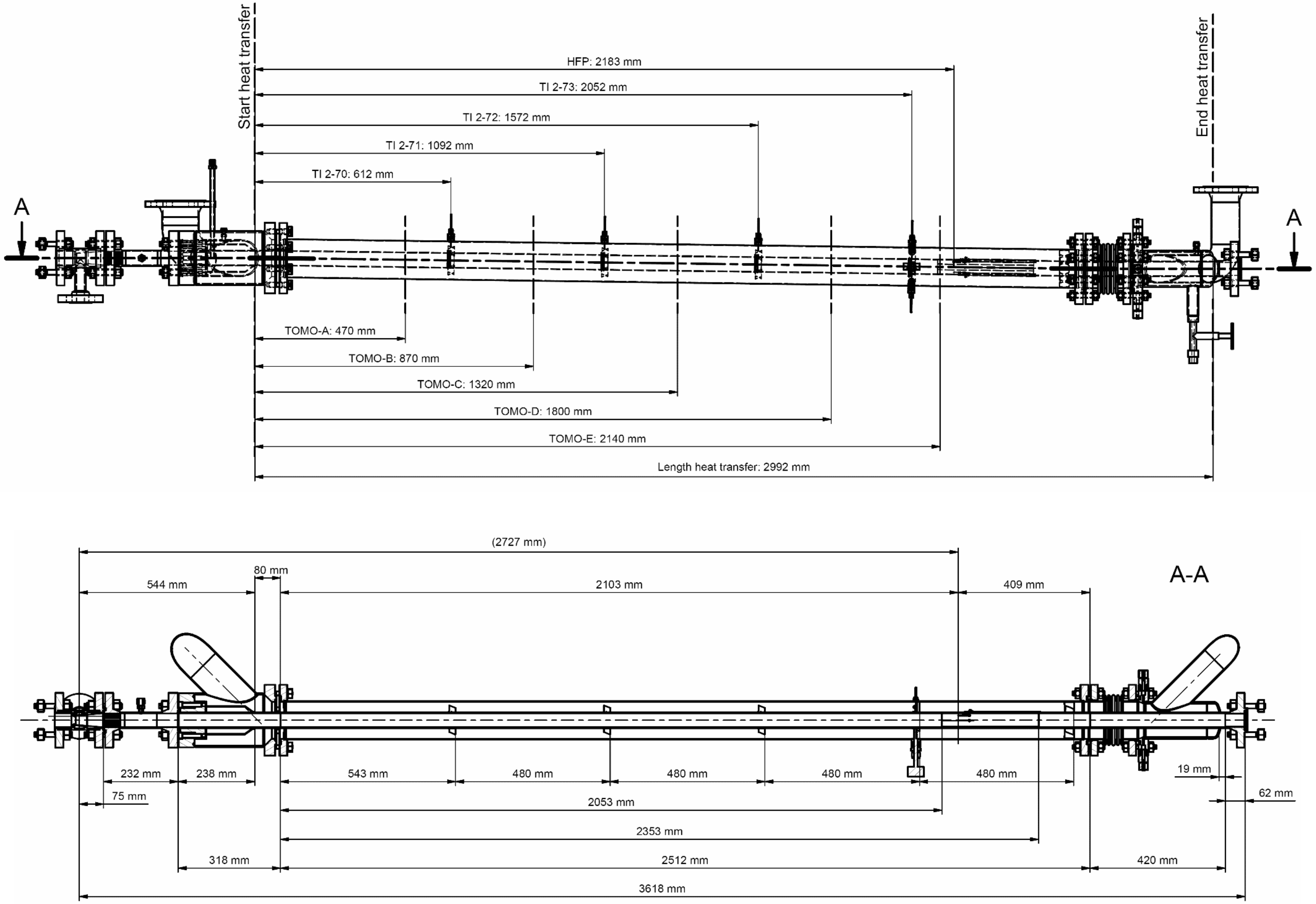

Figure 5: Longitudinal cut of the COSMEA test section: top: with locations of the instrumentation (TI – temperature measurement, HFP – heat flux probe, TOMO – tomographic imaging plane); bottom: with additional dimensions.

3.2 Inlet mixing system

The condensation process strongly depends on the flow regime inside the condenser tube. To investigate steam condensation over a wide range of void fraction either a long condenser tube is needed or alternatively, a well-defined two-phase flow must be fed in at the inlet. Due to limited space in the laboratory we reverted to the second option. Hence, a two-phase steam-water mixer has been designed and installed at the inlet of the horizontal test section (see Figure 6).

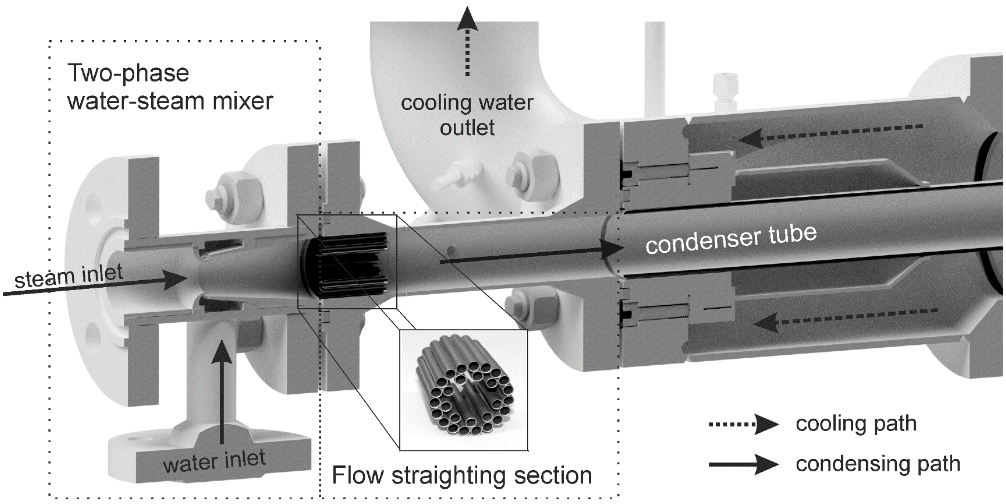

Figure 6: Two-phase steam-water flow mixer at the COSMEA facility.

It provides an annular liquid injection (annular gap width: 1.8 mm) into the condenser tube, which is close to an expected partially developed condensate film after some distance. However, as the tangential liquid injection causes an undesired swirling flow we additionally provided a so-called flow straightener downstream the mixer, which almost eliminates the swirling motion of the liquid. The flow straightener is fixed on the flange pair directly downstream the mixer by stainless steel clips. Between the mixer and the test section inlet, a plain tube segment with a total length of 225 mm is flanged. The flow straightener and the cooling water outlet module provide an adiabatic two-phase flow inlet length of 10 length-to-diameter ratio.

3.3 Condensation rate measurement

The condensation rate $\dot{m}_\mathrm{c}$ within the condenser tube can be derived using three different balancing approaches. They will be described in detail below. Enthalpies are denoted as H' and H'' for saturated water and saturated steam and as H_x for any specific stream x at absolute temperature T_x. To keep the notation as simple as possible we do not explicitly denote the pressure dependence of enthalpies. Hence enthalpies of saturated water H' and saturated steam $H"$ are to be taken at the actual system pressure. For practical calculations the enthalpies and further properties of water and steam were taken from FluidExcel©. For a better understanding of the following equations Figure 7 provides an overview of the physical parameters and their relation to local heat and mass fluxes in the facility. An explanation of the abbreviations is given after the equations.

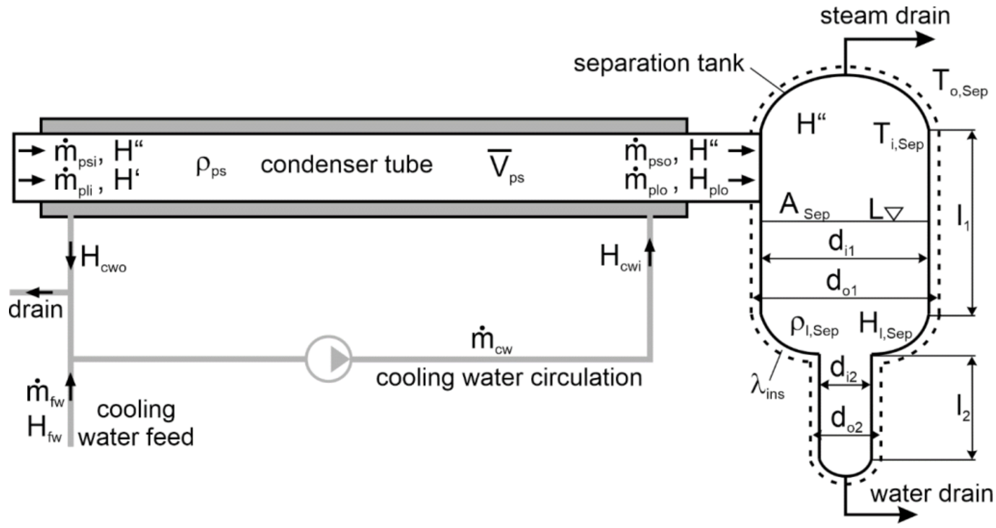

Figure 7: Scheme of the COSMEA test rig including the relevant geometry, heat and mass flux quantities used in equations (1) - (13).

Approach 1: The first approach considers the increase of enthalpy of the cooling water. The (rate of) heat transferred into the circulating cooling water on the secondary side is

$$\left(\frac{\Delta Q}{\Delta t}\right)_{\mathrm{cw}} = \dot{m}_{\mathrm{cw}}[H_{\mathrm{cwo}} - H_{\mathrm{cwi}})] \tag{1}$$

with the cooling water mass flux $\dot{m}_{\mathrm{cw}}$ and the enthalpy difference of the cooling water across the test section. On the primary side, the heat extraction leads to condensation as well as sub-cooling of condensate and injected saturated water, that is,

$$\left(\frac{\Delta Q}{\Delta t}\right)_{\mathrm{p}} = \dot{m}_{\mathrm{c}}\left[H" - H_{\mathrm{plo}}\right] + \dot{m}_{\mathrm{pli}}\left[H' - H_{\mathrm{plo}}\right]. \tag{2}$$

Here, $\dot{m}_{\mathrm{c}}$ is the condensate mass flux, $\dot{m}_{\mathrm{pli}}$ the mass flux of the liquid injected into the condenser tube, and H_{plo} the enthalpy of the sub-cooled water leaving the condenser tube. Balancing (1) and (2) one gets

$$\dot{m}_{\mathrm{c}}^{(1)} = \frac{\dot{m}_{\mathrm{cw}}[H_{\mathrm{cwo}} - H_{\mathrm{cwi}}] - \dot{m}_{\mathrm{pli}}\left[H' - H_{\mathrm{plo}}\right]}{H" - H_{\mathrm{plo}}} \tag{3}$$

The superscript “(1)” denotes, that this is the first out of three possible balancing approaches.

Approach 2: The temperature in the cooling circuit is controlled by the split-and-mix procedure as described above. This procedure gives way to a second approach of condensate rate quantification. Instead of using the secondary side circulation mass flux and enthalpies one may use the feed water mass flux $\dot{m}_{\mathrm{fw}}$ and the feed water enthalpy H_{fw}, that is,

$$\left(\frac{\Delta Q}{\Delta t}\right)_{\mathrm{fw}} = \dot{m}_{\mathrm{fw}}[H_{\mathrm{cwo}} - H_{\mathrm{fw}}]. \tag{4}$$

With that one obtains

$$\dot{m}_{\mathrm{c}}^{(2)} = \frac{\dot{m}_{\mathrm{fw}}[H_{\mathrm{cwo}} - H_{\mathrm{fw}}] - \dot{m}_{\mathrm{pli}}\left[H' - H_{\mathrm{plo}}\right]}{H" - H_{\mathrm{plo}}}. \tag{5}$$

Approach 3: As a third approach we consider the level increase rate dL/dt in the large cylindrical part (indicated as 1 in Figure 7) of the separation vessel downstream the condenser tube after an intermediate liquid drain line closure. For that, the condensation rate is

$$\dot{m}_{\mathrm{c}}^{(3)} = \frac{dL}{dt} A_{\mathrm{Sep}} \rho_{\mathrm{l,Sep}} - \dot{m}_{\mathrm{pli}} - \dot{m}_{\mathrm{hl}} - \dot{m}_{\mathrm{hu}} \tag{6}$$

with the cross-sectional area A_{Sep} of the separator vessel and the liquid density in the vessel $\rho_{\mathrm{l,Sep}}$. The mass flux term $\dot{m}_{\mathrm{hl}}$ accounts for condensation in the separator vessel due to heat losses and the term $\dot{m}_{\mathrm{hu}}$ accounts for steam condensation due to heat-up of sub-cooled water from the test section.

For the determination of the heat losses from the separation vessel we can start from the assumption that the 150 mm thick thermal insulation with thermal conductivity $\lambda_{\mathrm{ins}} = 0.047 - 0.059\ \mathrm{Wm^{-1}K^{-1}}$ (indeed it is a function of the mean insulation temperature) is the dominating thermal resistance. Hence, with reference to Figure 7, we can calculate the heat flux through the cylindrical parts (subscripts *cy,1* and *cy,2* for the large and small part respectively) and both torospherical heads (subscript *th*) by combining the heat conduction equations for cylindrical walls and hemispheric walls [39] as

$$\left(\frac{\Delta Q}{\Delta t}\right)_{\mathrm{hl}} = \lambda_{\mathrm{ins}} \left[\left(\frac{2\pi l_1}{ln \frac{d_{o1}}{d_{i1}}} \right)_{cy,1} + \left(\frac{2\pi l_2}{ln \frac{d_{o2}}{d_{i2}}} \right)_{cy,2} + \left(\frac{2\pi}{\frac{1}{d_{i1}} - \frac{1}{d_{o1}}} \right)_{th} \right] \left(T_{i,\mathrm{Sep}} - T_{o,\mathrm{Sep}}\right). \tag{7}$$

Here, d_i and d_o are the inner and outer diameter of the insulation shell (subscripts 1 – large and 2 – small respectively), $T_{i,\mathrm{sep}} - T_{o,\mathrm{sep}}$ is the temperature difference between the inner vessel atmosphere and the lab environment as well as l_1 and l_2 are the length of the large and small cylindrical part of the separation vessel respectively. In a further step we conservatively estimated the uncertainties due to unconsidered parts of the separation vessel, like e.g. instrumentation feed-throughs and steam blow-off pipe. From that we doubled the calculated value of the separation vessel heat losses. The last one can then be recalculated into a mass flux of condensed steam

$$\dot{m}_{\mathrm{hl}} = \frac{\left(\frac{\Delta Q}{\Delta t}\right)_{\mathrm{hl}}}{H^{"} - H_{l,\mathrm{Sep}}} \tag{8}$$

with $H_{l,\mathrm{Sep}}$ as the enthalpy of water at averaged liquid temperature inside the separator.

The last term in Eq. (6) accounts for the steam condensation in the separation tank due to heat-up of sub-cooled liquid from the test section, that is

$$\dot{m}_{\mathrm{hu}} = \frac{\left(\frac{\Delta Q}{\Delta t}\right)_{\mathrm{hu}}}{H^{"} - H_{l,\mathrm{Sep}}}. \tag{9}$$

and

$$\left(\frac{\Delta Q}{\Delta t}\right)_{\mathrm{hu}} = \dot{m}_{\mathrm{plo}}\left[H_{l,\mathrm{Sep}} - H_{\mathrm{plo}}\right]. \tag{10}$$

As

$$\dot{m}_{\mathrm{plo}} = \dot{m}_{\mathrm{c}}^{(3)} + \dot{m}_{\mathrm{pli}}, \tag{11}$$

we get

$$\dot{m}_{\mathrm{hu}} = \left(\dot{m}_{\mathrm{c}}^{(3)} + \dot{m}_{\mathrm{pli}}\right)\frac{H_{l,\mathrm{Sep}} - H_{\mathrm{plo}}}{H^{"} - H_{l,\mathrm{Sep}}}. \tag{12}$$

Inserting (12) into (6) and rearranging for $\dot{m}_{\mathrm{c}}^{(3)}$ gives

$$\dot{m}_{\mathrm{c}}^{(3)} = \frac{\frac{dL}{dt}A_{\mathrm{Sep}}\rho_{\mathrm{l,Sep}} - \dot{m}_{\mathrm{hl}}}{\left(1 + \frac{H_{l,\mathrm{Sep}} - H_{\mathrm{plo}}}{H^{"} - H_{l,\mathrm{Sep}}}\right)} - \dot{m}_{\mathrm{pli}}. \tag{13}$$

While the 1st and 2nd approaches result in an exact calculation of the condensation rate, the 3rd one includes some assumption and corrections about heat losses and is therefore prone to slightly higher uncertainties. Hence, the 3rd method was used for plausibility cross-comparison only. To examine the quality of both energy balance methods their uncertainties were calculated, applying the law of uncertainty propagation for Eq. (3) and Eq. (5). The structure of both equations is similar, so only the calculation of the 1st approach is presented here:

$$\Delta \dot{m}_{\mathrm{c}}^{(1)} = \sqrt{\begin{gathered} \left(\frac{H_{\mathrm{cwo}} - H_{\mathrm{cwi}}}{H'' - H_{\mathrm{plo}}} \cdot \Delta \dot{m}_{\mathrm{cw}}\right)^2 + \left(\frac{\dot{m}_{\mathrm{cw}}}{H'' - H_{\mathrm{plo}}} \cdot \Delta H_{\mathrm{cwo}}\right)^2 + \left(\frac{-\dot{m}_{\mathrm{cw}}}{H'' - H_{\mathrm{plo}}} \cdot \Delta H_{\mathrm{cwi}}\right)^2 + \\ \left(-\frac{H' - H_{\mathrm{plo}}}{H'' - H_{\mathrm{plo}}} \cdot \Delta \dot{m}_{\mathrm{pli}}\right)^2 + \left(\frac{-\dot{m}_{\mathrm{pli}}}{H'' - H_{\mathrm{plo}}} \cdot \Delta H'\right)^2 + \left(\frac{\dot{m}_{\mathrm{pli}}}{H'' - H_{\mathrm{plo}}} \cdot \Delta H_{\mathrm{plo}}\right)^2 + \\ \left(\frac{-\left[\dot{m}_{\mathrm{cw}} \cdot (H_{\mathrm{cwo}} - H_{\mathrm{cwi}}) - \dot{m}_{\mathrm{pli}} \cdot (H' - H_{\mathrm{plo}})\right]}{\left(H'' - H_{\mathrm{plo}}\right)^2} \cdot \Delta H''\right)^2 + \\ \left(\frac{\left[\dot{m}_{\mathrm{cw}} \cdot (H_{\mathrm{cwo}} - H_{\mathrm{cwi}}) - \dot{m}_{\mathrm{pli}} \cdot (H' - H_{\mathrm{plo}})\right]}{\left(H'' - H_{\mathrm{plo}}\right)^2} \cdot \Delta H_{\mathrm{plo}}\right)^2 \end{gathered}} \tag{14}$$

Both uncertainty calculations are based on individual uncertainties of single parameters listed in Table 2.

Table 2: Individual uncertainties of all parameters used for condensation rate and heat flux calculation.

Parameter	**Pressure [bar]**	**Uncertainty**	**Reference**
m_{cw}, m_{fw}		±1%	Swirl flow meter, TOPFLOW documentation
m_{pli}		±0.2%	Coriolis flow meter, TOPFLOW documentation
m_{psi} (FIC4-05)		±2.1%	Orifice plate, TOPFLOW documentation
m_{psi} (FIC4-04)		±2.2%	Orifice plate, TOPFLOW documentation
H_{cwo}, H_{cwi}, H_{fw}		±1.24%	Individual uncertainties of pressure and temperature measurement and of IAPWS IF97
H', H"	5 12 25 45 65	±0.95% ±0.85% ±0.76% ±0.67% ±0.58%	Individual uncertainties of pressure measurement depending on test conditions and of IAPWS IF97
H_{plo}	5 12 25 45 65	±0.97% ±0.87% ±0.77% ±0.68% ±0.59%	Individual uncertainties of pressure and temperature measurement depending on test conditions and of IAPWS IF97
T_{wi}, T_{wo}		±0.3 K	After thermal calibration and polynomial correction
λ		± 7%	VDI-Wärmeatlas 2013, section D6, page 630
δ		±0.15 mm	0.1 mm from ultrasonic device and 0,05 mm from confocal white-light microscopy
ρ_{ps}	5 12 25 45 65	0.9% 0.8% 0.7% 0.6% 0.5%	Individual uncertainty of pressure measurement depending on test conditions and of IAPWS IF97

The uncertainty analysis showed that the 1st approach has a significantly higher uncertainty due to the fact that the mass flow of circulating cooling water is relatively high. Hence we consider the 2nd approach as best for condensation rate estimation. Results including uncertainties are presented in chapter 4.2.

3.4 Wall heat flux measurement

The wall heat flux $\dot{q}_\mathrm{w}$ through the condenser tube wall is determined from the temperature difference $T_\mathrm{wi} - T_\mathrm{wo}$ measured by pairs of thermocouples at the inner (primary side) and outer (secondary side) condenser tube wall according to

$$\dot{q}_\mathrm{w} = \lambda(\bar{T}) \frac{T_\mathrm{wi} - T_\mathrm{wo}}{\delta}. \qquad (15)$$

Here, δ is the distance between the thermocouples and $\lambda(\bar{T})$ is the thermal conductivity of the wall material (stainless steel) at mean wall temperature [39]. Thermocouple pairs are arranged in five circumferential positions (0°, 45°, 90°, 135° 180°) as shown in Figure 8. This arrangement provides the circumferential heat flux with some angular resolution and particularly allows discrimination of heat flux from the steam and the condensate (bottom part) through the wall. As the inlet flow straightener provides a good axis-symmetric inlet flow we considered a thermocouple pair arrangement in only one half of the cross-section as sufficient. This assumption of flow symmetry has been confirmed by the X-ray measurements.

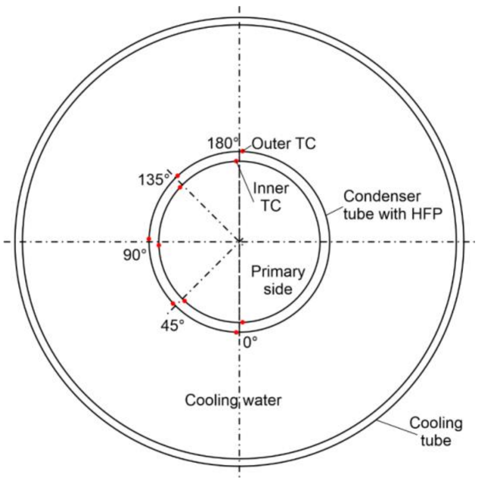

Figure 8: Schema of TC arrangement on the heat flux probe (HFP).

We employed thermocouples of Type K class 1 with a sensor tip diameter of 0.5 mm. They are spot-welded in eroded grooves with a depth of 250 µm to minimize the influence of the near-wall fluid temperature. For reasons of mechanical stability the grooves on the outer wall are 4° displaced against the grooves at the inner wall. As the true distance δ of each thermocouple pair is important for accurate heat flux measurement it was determined before the test section assembly by measuring the condenser tube wall thickness at each position using an ultrasonic inspection technique and measuring the thermocouple immersion depth using confocal white light microscopy. To assess the quality of the heat flux measurement, their uncertainty was determined using the law of error propagation to Eq. (14). From this one gets

$$\Delta\dot{q}_{\mathrm{w}} = \sqrt{\left(\frac{T_{\mathrm{wi}} - T_{\mathrm{wo}}}{\delta} \cdot \Delta\lambda\right)^2 + \left(\frac{\lambda}{\delta} \cdot \Delta T_{\mathrm{wi}}\right)^2 + \left(-\frac{\lambda}{\delta} \cdot \Delta T_{\mathrm{wo}}\right)^2 + \left(-\frac{\lambda \cdot (T_{\mathrm{wi}} - T_{\mathrm{wo}})}{\delta^2} \cdot \Delta\delta\right)^2}. \tag{16}$$

The individual uncertainties and their references are taken from Table 2. The uncertainty of the heat flux is dominated by the 1st and 4th term in Eq. (16), respectively the individual uncertainties of the thermal conductivity and the wall thickness. Since both terms in Eq. (16) mainly depend on the temperature difference between the primary and secondary wall side and the heat flux itself shows the same dependency, the heat flux relative uncertainty is practically independent of the operational boundary condition. It was found approximately at 9%. Similar to the previous section the results of the circumferentially distributed heat flux and their uncertainties are presented in section 4.3.

3.5 X-ray tomography

3.5.1 CT setup and data processing

The COSMEA facility is equipped with a proprietary X-ray computed tomography (CT) system that enables non-invasive imaging of the cross-sectional liquid fraction distribution along the entire condenser tube section (see Figure 9). The CT scanner comprises a rotating frame with an X-ray source, a radiation flat panel detector (1024×1024 pixels of 400×400 µm² active area) and a control unit. The X-ray source is collimated by means of adjustable lead plates in front of the beam exit window to suppress scattered radiation by at least one order of magnitude. Moreover, the whole CT system can be automatically traversed along the whole test section. For cross-sectional scanning a servo-motor drives the source-detector assembly around the condenser tube section in an angular range of about 230°. Every 0.36° an X-ray image is taken with an exposure time of 100 ms. From a set of 640 projection images (total scanning time approx. 10 min) a computer program reconstructs the cross-sectional images. For that we implemented a numerical inverse Radon transformation in GNU OCTAVE v4.2.1. The whole data processing and image reconstruction comprises the following single steps:

- Dark field subtraction to compensate for the detector’s dark current
- Attenuation value calculation using a reference CT scan without object
- Defective pixel correction by linear interpolation from non-defective neighbour pixels

- Scattered radiation correction using an approximation of the scattered radiation intensity profile fitted to measured intensities behind the X-ray source collimator edges
- Correction of electrical crosstalk between the detector module panels
- Averaging of projection data over 61 detector lines corresponding to an averaging along an effective axial distance of 8.5 mm in the test section
- Correction of the condenser tube position within the fan beam projection data
- Interpolation from fan beam to parallel beam projection data
- Reduction of the projection data to the essential 180° parallel beam projection
- Clipping of the parallel beam projection data so that it contains the condenser tube only

As the CT scanning interval is rather long it was decided to limit tomography to five equally spaced axial positions along the test section. The exact positions are selected in places, where images are least distorted by extra materials, such as thermocouples or swirling elements in the cooling tube. For that we initially performed a frontal radiographic scan of the inactive test section and determined the five axial CT scanning positions denoted as “A”-“E” shown in Figure 10 (A: 470 mm, B: 870 mm, C: 1320 mm, D: 1800 mm, E: 2140 mm).

Figure 9: COSMEA facility at HZDR with the X-ray CT scanner.

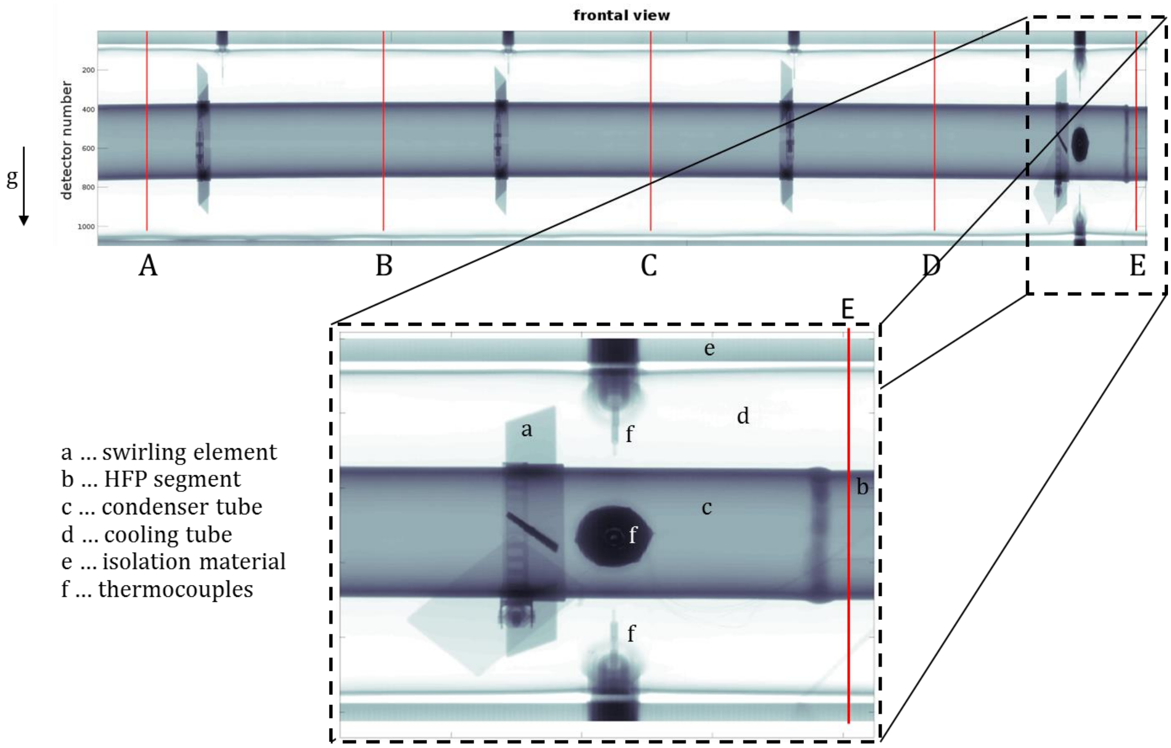

Figure 10: Frontal radiographic scan of the inactive COSMEA facility with determined CT scanning positions “A”-“E” (top) and detailed information (bottom).

3.5.2 Assessment of the CT measurement uncertainty

As our X-ray CT imaging system is custom-made we initially determined the measuring uncertainty by means of a phantom experiment. The phantom (Figure 11a) resembles a water film of increasing thickness at the inner tube wall. It comprises of two hollow steel cylinders resembling the outer and inner tube walls with the annulus being completely filled with casting resin to model the cooling water. A stack of four silicone stripes, representing static condensate films of thickness between 1 mm and 4 mm is placed on the inner wall of the condenser tube section. Finally, the phantom was jacketed with mineral wool insulation material. The following CT scanning parameters have been experimentally determined as optimal with respect to detector exposure and total scanning time:

- Tube voltage: 150 keV
- Tube power: 3.75 kW
- Focal spot size: 0.6 mm
- Exposure interval: 100 ms (power controlled)

The resulting reconstructed cross-sectional image of the phantom is shown in Figure 11. As it can be seen in the corresponding extracted averaged and normalized attenuation profiles in Figure 11b, the

1 mm silicon stripe can still be visualized with approx. 80% of its contrast. It indicates that the resolution ability for a condensation film near the condenser inner wall is better than 1 mm.

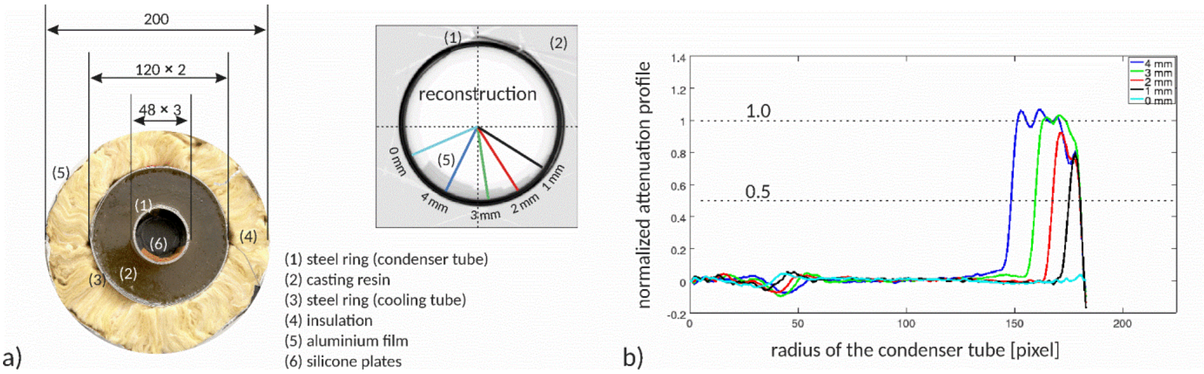

Figure 11: Assessment of the uncertainty for X-ray imaging based liquid film thickness measurement. a) Phantom that resembles a section of the concentric tubes with a liquid film of different thickness inside. b) Extracted normalized attenuation profiles of the silicone stacks.

A more appropriate measure for the contrast resolution is the modulation transfer function (MTF) of the imaging system. It has been determined from a CT scan of a quiescent liquid level in the tube. Therefore, the condenser tube was filled with deionized water and all valves were closed. The trapped stratified deionized water develops a sharp static interface and the resulting edge at the interface in the cross-sectional images can be used to calculate the MTF for the present setup from the attenuation profiles along the vertical diameter, which were evaluated for different filling levels denoted at cross-section “C” (1320 mm), “D” (1800 mm) and “E” (2140 mm) (see Figure 12). The filling level represents an edge and the CT scanner obtains an image which contains the edge response function. From that the point spread function can be de-convolved, whose Fourier transform is the MTF. The resulting MTF gives a resolution of 1.43 line pairs per millimeter at 50% contrast $C(0.5)$, which in turn indicates a detectability of an interface for a film of a thickness down to 0.5 mm. From the evolution of the quiescent gas-liquid interface along the tube axis in the X-ray images we were able to measure the real inclination angle of the condenser tube as 0.88 ±0.035°. The uncertainty comes from the spatial resolution (~0.5 mm). Note, that the inclination difference between the nominal value (0.76°) and the measured mean value (0.88°) corresponds to about 7.2 mm difference in height of the rightmost point of the condenser tube. The difference is due to both manufacturing tolerances and the loose-fit fixation of the downstream part of the condenser tube. Further note, that thermal expansion of the tube during experiments does give another inclination offset of up to 0.06° or 1.8 mm (section 3.5.6, Figure 14).

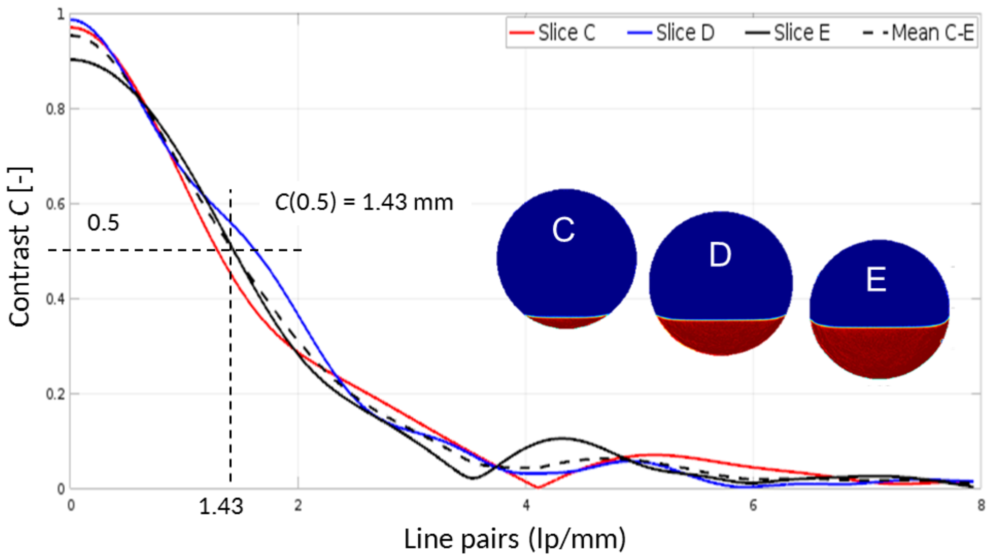

Figure 12: Modulation transfer function of the X-ray CT imaging system (for details see text).

3.5.3 CT data analysis

Ideally, the image reconstruction delivers cross-sectional images, i.e. 2D maps, of the linear attenuation coefficient of the materials in the cross-section. They will be further denoted by $\mu(x,y)$ with an additional index for a particular data set from an experiment (*exp*) or a reference measurement. In principle, the linear attenuation coefficient is linearly proportional to the material density. This allows a quantitative analysis of the liquid distribution. However, the reconstruction of absolute linear attenuation coefficients is prone to a number of uncertainties associated with the X-ray propagation and image reconstruction. Therefore, it is common practice to employ differential measurements, that is, scaling the reconstructed values $\mu_{\mathrm{exp}}(x,y)$ of a given experiment with reference values for the tube being filled once completely with gas $\mu_{\mathrm{g}}(x,y)$ and once completely with liquid $\mu_{\mathrm{l}}(x,y)$. If such references are available, the quantitative liquid fraction distribution can be calculated

$$\alpha(x,y) = \frac{\mu_{\mathrm{exp}}(x,y) - \mu_{\mathrm{g}}(x,y)}{\mu_{\mathrm{l}}(x,y) - \mu_{\mathrm{g}}(x,y)} \cdot \frac{\rho_{\mathrm{l}} - \rho_{\mathrm{g}}}{\rho_{\mathrm{exp}} - \rho_{\mathrm{g}}}. \tag{17}$$

The second term at the right-hand side accounts for density differences between experiment and reference scan due to temperature differences. This procedure is e.g. fully described in [40].

It has been found, however, that the procedure described above is not straightforwardly applicable to COSMEA experiments. Thus, the geometrical displacements of the tube between images taken at different temperatures leads to strong artefacts in the images. Even when applying displacement correction by means of image processing (e.g. by geometrical shifting of the tube in the images) such artefacts cannot be fully removed, especially in the near-wall regions, which are important for analysis. Moreover, for technical reasons it is very difficult to fill the tube completely with saturated water and keep the water on saturation temperature during X-ray scans. Hence, we reverted to a modified scaling approach. First of all we performed reference scans for the gas-filled tube (μ_g) and the liquid-filled tube (μ_l) at ambient conditions (1 bar, 20°C). Next we performed a third reference scan for the maximum possible steam flow at given experimental conditions (pressure, saturation temperature). The resulting image is referred to as μ_s^*. The asterisk indicates the reference to the values given in Table 3. Note, that the difference images, $\mu_\mathrm{exp}(x,y) - \mu_\mathrm{s}^*(x,y)$ and $\mu_\mathrm{l}(x,y) - \mu_\mathrm{g}(x,y)$, are free of displacement artifacts, as the individual scans have been performed at the same temperature and pressure stages. However, they still have a displacement against each other. When we now perform a shift correction by automatic image processing, the resulting liquid fraction image (see Eq. (18)) is no more corrupted. Thereby, $\mu_\mathrm{s}^*(x,y)$ can be considered as a reference for a fully steam-filled tube. However, as the tube wall is slightly sub-cooled we may expect a small condensate film at the inner wall side. To ensure that this does not introduce additional uncertainties we assessed all reconstructed cross-sectional images with a visible bottom condensate flow, if there is a negative gray value gradient towards the wall in the condensate region. We could confirm that this is not the case, from which it follows that a) the condensate film is well below the resolution limit (~0.5 mm) of the X-ray tomography and b) does therefore not introduce uncertainty in the near-wall region.

Eventually, we obtain the liquid fraction by further correcting with the density differences as

$$\alpha_\mathrm{CT}(x,y) = \frac{\mu_\mathrm{exp}(x,y) - \mu_\mathrm{s}^*(x,y)}{\mu_\mathrm{l}(x,y) - \mu_\mathrm{g}(x,y)} \cdot \frac{\rho_\mathrm{l} - \rho_\mathrm{g}}{\rho_\mathrm{exp} - \rho_\mathrm{s}} \tag{18}$$

and correspondingly the steam fraction as

$$\varepsilon_\mathrm{CT}(x,y) = 1 - \alpha(x,y). \tag{19}$$

The condensate height L_c can be directly taken from the central vertical attenuation profile of the reconstructed slice as shown in Figure 13a. To improve accuracy a centrally placed profile thickness of $\delta_\mathrm{profil} = 1\ \mathrm{mm}$ is used. As liquid fraction threshold value $\alpha = 0.5$ is used for this parameter. As the steam-liquid interface is agitated by the gas-liquid shear and turbulent structures wave structures are developed. Though those cannot be resolved in time the wave amplitude can be quantified via the liquid fraction transition zone at the interface in the reconstructed images. For that the transition zone width ΔL is extracted by defining lower and upper thresholds $\alpha = 0.1$ and $\alpha = 0.9$. The corresponding condensate level heights L_c^- and L_c^+ are than used to compute the transition zone $\Delta L = L_\mathrm{c}^- - L_\mathrm{c}^+$, as shown in Figure 13b. The accuracy has been determined as ±0.13 mm.

The total liquid fraction in the cross-section can directly be computed from the CT image according to

$$\bar{\alpha}_{\mathrm{CT}} = \frac{1}{N_x N_y} \sum_{x=1}^{N_x} \sum_{y=1}^{N_y} w(x,y)\alpha(x,y). \tag{20}$$

and the total steam fraction as well

$$\bar{\varepsilon}_{\mathrm{CT}} = 1 - \bar{\alpha}_{\mathrm{CT}}. \tag{21}$$

The weight function $w(x,y)$ defines the share of the pixel with the internal cross-section of the tube, that is, $w(x,y) = 0$ for pixels outside the tube cross-section, $w(x,y) = 1$ for pixels inside and $0 < w(x,y) < 1$ for pixels on the boundary.

Moreover, from geometrical considerations of a well separated flow with a flat interface the following relationship between total liquid fraction $\bar{\alpha}_{\mathrm{L}}$ and liquid level L_{c} can be derived by

$$\bar{\alpha}_{\mathrm{L}} = \frac{A_{\mathrm{r}}}{A_{\mathrm{i}}} = \frac{\frac{1}{2} \cdot (r_{\mathrm{i}} \cdot b - s \cdot (r_{\mathrm{i}} - L_{\mathrm{c}}))}{\pi \cdot r_{\mathrm{i}}^2}. \tag{22}$$

Here, A_{r} denotes the flume cross-sectional area and A_{i} the inner cross-sectional area of the tube. The other geometrical parameters are given in Figure 13. Although, the total liquid fraction $\bar{\alpha}_{\mathrm{CT}}$ that is directly computed from the CT image is more appropriate for a non-flat interface, this second method that considers the stratified condensate level (SCL) has been used for cross-comparison.

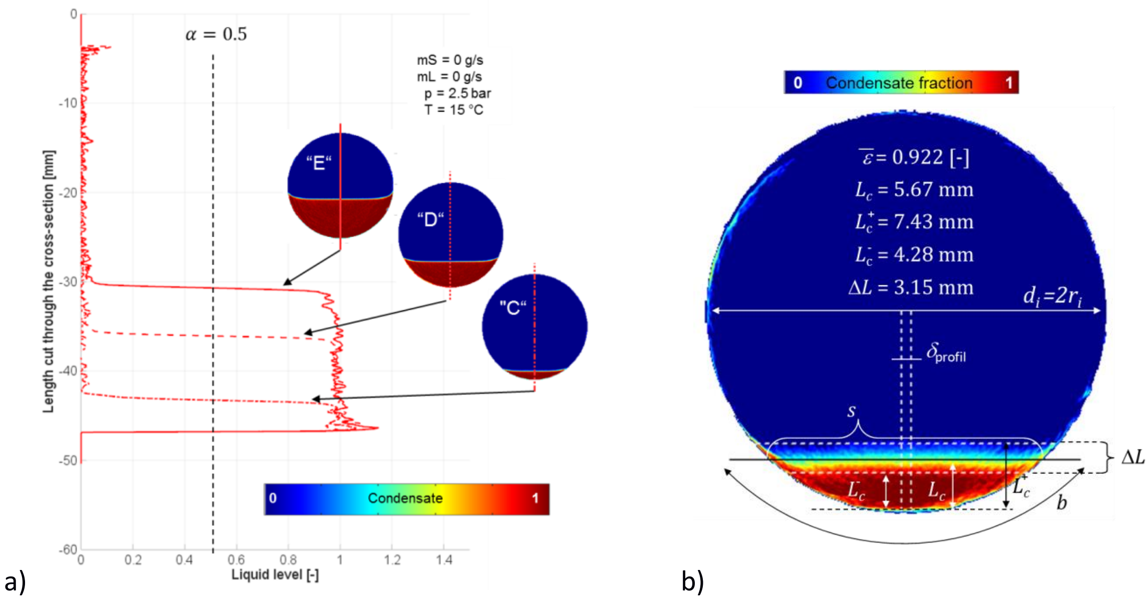

Figure 13: Procedure to investigate a) the height and b) the transition zone of the stratified condensate (flume) from the cross-sectional X-ray CT images.

3.5.4 Displacement of the condenser tube due to thermal expansion

Due to thermal expansion the inclination angle of the test section changes slightly at different operating conditions, which may have to be considered in forthcoming numerical simulations. The displacement increases with temperature and axial distance from the separation vessel, as the latter is a fix-point of the condenser tube. Thus, we used the tomographic images to determine the vertical and horizontal displacement by determining the centre position of the condenser tube in Section "A" and "E", calculating the centre shift offset against the centre positions given in chapter 3.5. As expected the largest displacement was found at CT position "A" at maximal pressure difference of 65 bar, and is exemplarily shown as an inset in Figure 14. Moreover the displacement is fortunately stronger in horizontal direction and therefore, the inclination angle change is less affected. The results are summarized graphically in Figure 14 and quantitatively in Table 3.

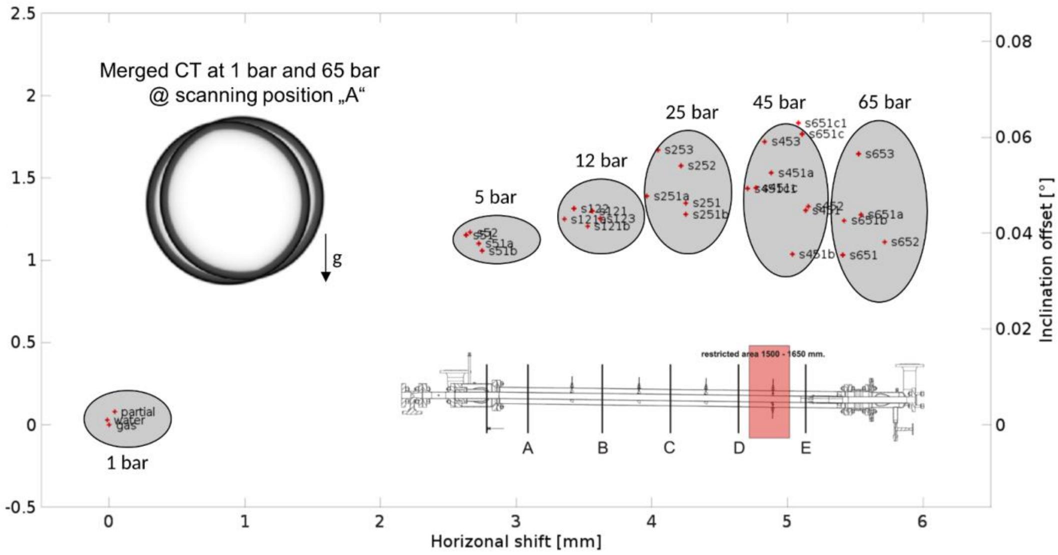

Figure 14: Vertical and horizontal displacement of the condenser tube at different operating points (pressure stages) as obtained from the reconstructed cross-sectional images between CT scanning position "A" and "E".

4. Results and discussion

4.1 Test matrix and experimental procedure

Experiments were performed for the conditions given in Table 3. Grey cells indicate experiments with additional injection of saturated water (two-phase mixture at inlet).

Table 3: Summary of the basic experimental conditions (*indicates reference CT scan for corresponding pressure stage, grey cells indicate experiments with additional injection of saturated water).

Test #	p_{p} [bar(a)]	$\dot{m}_{\mathrm{total}}$ [kg/s]	$\dot{m}_{\mathrm{psi}}$ [kg/s]	$\dot{m}_{\mathrm{pli}}$ [kg/s]	T_{pli} [°C]	p_{cw} [bar(a)]	$\dot{m}_{\mathrm{cw}}$ [kg/s]	T_{cwi} [°C]	T_{cwo} [°C]	Inclination offset [°]
s51	5.004	0.0795	0.0795	0		3.110	13.38	44.3	46.6	+0.040
s51a	5.010	0.1195	0.1195	0		3.132	13.45	43.5	45.9	+0.038
s51b*	5.015	0.1510	0.1510	0		3.120	13.56	44.2	46.5	+0.036
s52	5.008	0.0985	0.0585	0.040	151.9	3.187	13.33	44.9	47.0	+0.040
s121	12.008	0.1834	0.1834	0		3.138	13.62	43.9	47.2	+0.045
s121a	12.007	0.0996	0.0996	0		3.139	13.58	44.2	47.1	+0.043
s121b	12.028	0.2797	0.2797	0		3.188	13.65	43.4	47.0	+0.041
s122	12.006	0.1850	0.1400	0.045	183.0	3.173	13.57	44.2	47.4	+0.045
s123	12.006	0.1821	0.1021	0.080	187.6	3.145	13.58	44.0	47.0	+0.043
s251	25.058	0.3723	0.3723	0		3.127	13.77	43.3	47.8	+0.046
s251a	25.040	0.1707	0.1707	0		3.149	13.57	42.9	46.5	+0.048
s251b	25.093	0.5536	0.5536	0		3.218	15.86	43.7	48.0	+0.044
s252	25.053	0.3711	0.2331	0.138	223.7	3.169	13.74	43.3	47.4	+0.054
s253	25.050	0.3720	0.1240	0.248	224.5	3.158	13.64	43.6	47.3	+0.057
s451	45.094	0.6739	0.6739	0		3.340	19.44	43.5	47.8	+0.045
s451a	45.056	0.2492	0.2492	0		3.249	15.38	43.2	47.5	+0.053
s451b	45.289	1.0039	1.0039	0		3.480	20.95	42.9	47.2	+0.036
s451c	45.056	0.1528	0.1528	0		3.187	13.64	43.8	47.8	+0.049
s452	45.064	0.6727	0.4197	0.253	257.7^{+}	3.319	18.19	43.4	47.7	+0.046
s453	45.048	0.6742	0.2042	0.470	259.2^{+}	3.278	16.13	43.5	47.8	+0.059
s651*	65.161	1.0038	1.0038	0		3.590	23.40	43.0	47.3	+0.035
s651a	65.107	0.3493	0.3493	0		3.355	18.73	43.3	47.6	+0.044
s651b	65.121	0.6785	0.6785	0		3.462	21.94	43.8	48.1	+0.043
s651c	65.104	0.1965	0.1965	0		3.208	14.41	43.3	47.6	+0.061
s652	65.126	1.0006	0.6226	0.378	281.3^{+}	3.500	22.18	43.3	47.6	+0.038
s653	65.164	0.9937	0.2427	0.751	284.3^{+}	3.347	19.54	43.4	47.6	+0.056

The description of the parameters in Table 3 corresponds to the nomenclature introduced in Figure 7 and in Eq. (1) - (15). The liquid temperatures at condensation tube inlet (T_{pli}) marked with a ($^{+}$) are slightly higher than the saturation temperature at primary pressure (p_{p}). This is due to pressure drop over the annular gap of the mixer at condensation tube inlet (see Figure 6) that causes a low overpressure at temperature measurement position T_{pli}. Saturated steam mass flows up to 1.00 kg/s and water mass flows up to 0.75 kg/s resulting in inlet mass steam fractions between 0.244 and 1.000 that have been studied at steady-state conditions.

At the beginning of each experimental campaign the COSMEA test rig was heated up by starting and regulating the cooling water circulation loop. Then steam from the TOPFLOW steam generator was injected into the condensation tube with a mass flow higher than the condensation rate. Thereby, the drain-line of the separation tank was opened to blow-off the residing mixture of air, steam and condensate. This procedure allows an effective way to degas the test section and the separation vessel, which is a basic requirement for high quality condensation tests without non-condensable gases. The degassing was concluded when the gas temperature inside the separation vessel was at saturation temperature for the given pressure. During steam injection the primary side of the test rig was heated up until the pressure set value was slightly exceeded. This operation accelerates the temperature rise in the COSMEA steel components. Afterwards, the drain line was partly closed and a low constant level in the large part of the separation vessel was adjusted. Besides, the experimental conditions (Table 3) were adjusted too and stabilized over 15 min to give stable steady-state conditions. The pressure in the test rig was controlled automatically by regulation of the blow-off steam flow. When all parameters were properly adjusted the CT scans were conducted at constant level in the separation vessel. After this the condensate drain line of the separation tank was completely closed to determine the level gradient for the condensation rate calculation.

As aforementioned, all tests described here were run in steady-state conditions. For the perpetuation of constant thermal hydraulic conditions we used two control mechanisms. In the cooling circuit we applied the above described feed-and-split procedure to adjust the circulating flow at almost constant temperature, independent of the transferred heat. On the primary side we had to control the pressure under condensation conditions. Note that beside the investigated condensation of steam in the condenser tube, there is also “parasitic” condensation of steam in the separation vessel due to heat losses through its wall and heat-up of sub-cooled condensate from the condenser tube in the separation tank. Both effects were explained and quantified in section 3.3. Furthermore, a small amount of additional steam has to be continuously fed into the separation tank to replace steam losses from pressure-controlling steam blow-offs.

4.2 Condensation rate

The results of the condensation rate $\dot{m}_{\mathrm{c}}$ calculation regarding to section 3.3 for all experiments including their uncertainties are presented in Table 4. For a better overview $\dot{m}_{\mathrm{c}}$ was plotted in two diagrams, at the one hand as a function of mean steam mass fraction $\bar{x}$ (Figure 15a) and at the other hand subject to the mean steam volumetric flow rate, averaged over the condensation tube length (Figure 15b). Mean values were chosen because the condensation rate represents an integral characteristic over the entire condensation domain. The inlet steam fraction was calculated as

$$\bar{x} = \frac{2 \cdot \dot{m}_{\mathrm{psi}} - \dot{m}_{\mathrm{c}}^{(2)}}{2 \cdot (\dot{m}_{\mathrm{psi}} + \dot{m}_{\mathrm{pli}})}. \qquad (23)$$

In Eq. (23), $\dot{m}_{\mathrm{psi}}$ is the steam mass flow injected into the primary side of the condensation tube. The mean steam volumetric flow rate was determined as

$$\bar{\dot{V}}_{\mathrm{ps}} = \frac{2 \cdot \dot{m}_{\mathrm{psi}} - \dot{m}_{\mathrm{c}}^{(2)}}{2 \cdot \rho_{\mathrm{ps}}}. \qquad (24)$$

Here ρ_{ps} stands for the primary side steam density. For a correct visualization an uncertainty analysis for both steam mass fraction and steam mass flow rate was performed (Table 4). Similar to section 3.3 the law of uncertainty propagation was applied to Eq. (23) and Eq. (24). The individual uncertainties of the raw data were taken from Table 2.

Table 4: Condensation rates (calculated by the 2nd approach explained in section 3.3).

Test #	$\bar{x}$ **[-]**	$\bar{\dot{V}}_{ps}$ **[m³/h]**	$\dot{m}_c^{(2)}$ **[g/s]**		**Test #**	$\bar{x}$ **[-]**	$\bar{\dot{V}}_{ps}$ **[m³/h]**	$\dot{m}_c^{(2)}$ **[g/s]**
s51	0.642 ±0.022	68.8 ±3.2	57 ±3.3		**s451**	0.844 ±0.011	90.0 ±2.6	210 ±13.5
s51a	0.728 ±0,017	117.2 ±4.4	65 ±3.9		**s451a**	0.687 ±0.019	27.1 ±1.1	156 ±9.1
s51b*	0.775 ±0.016	157.3 ±5.4	68 ±4.4		**s451b***	0.888 ±0.006	140.4 ±3.7	225 ±11.7
s52	0.331 ±0.017	43.9 ±2.5	52 ±2.8		**s451c**	0.607 ±0.023	14.7 ±0.7	120 ±6.4
					s451c1	0.608 ±0.021	14.9 ±0.7	121 ±6.1
s121	0.746 ±0.016	80.4 ±3.0	93 ±5.6		**s452**	0.483 ±0.011	51.5 ±1.7	189 ±11.5
s121a	0.608 ±0.025	35.6 ±1.9	78 ±4.7		**s453**	0.203 ±0.009	21.7 ±1.0	134 ±9.5
s121b*	0.816 ±0.012	133.9 ±4.2	103 ±6.1					
s122	0.524 ±0.015	57.0 ±2.3	86 ±4.8		**s651***	0.863 ±0.008	92.5 ±2.5	275 ±14.8
s123	0.349 ±0.015	37.4 ±1.9	77 ±4.8		**s651a**	0.708 ±0.016	26.4 ±1.0	204 ±10.3
					s651b	0.811 ±0.016	58.7 ±2.0	257 ±21.6
s251	0.811 ±0.012	86.7 ±2.7	141 ±8.6		**s651c**	0.634 ±0.018	13.3 ±0.6	144 ±6.5
s251a	0.687 ±0.016	33.7 ±1.3	107 ±4.8		**s651c1**	0.633 ±0.020	13.3 ±0.6	144 ±6.9
s251b*	0.860 ±0.012	136.5 ±4.0	155 ±12.5		**s652**	0.498 ±0.010	53.2 ±1.7	249 ±14.1
s252	0.462 ±0.013	49.3 ±1.9	123 ±7.9		**s653**	0.159 ±0.009	16.9 ±1.0	169 ±15.4
s253	0.210 ±0.010	22.4 ±1.2	92 ±6.1					

Figure 15a shows the influence of the liquid content in the horizontal tube on the condensation rate. The condensation rate decreases with decreasing mean steam mass fraction. This effect is attributed to the fact that liquid blocks direct steam contact to the bottom part of the inner tube wall and therefore lowers an effective heat transfer.

In Figure 15b the condensation rates (2nd approach) for experiments with pure steam injection are plotted against the mean steam volumetric flow rate. The strong influence of steam flow, respectively the averaged steam velocity, on the condensation rate is clearly recognizable. As for example, reducing the steam flow from 92.5 m³/h to 13.3 m³/h at 65 bar halves the condensation rate at no change of any other operational boundary condition. This effect bases on a decrease of the primary heat transfer coefficient due to a decrease of the steam velocity. Both diagrams in Figure 15 clearly show the influence of the pressure in the condensation. As expected from the increasing temperature difference between cooling water and steam, the condensation rates increase with system pressure at comparable boundary condition.

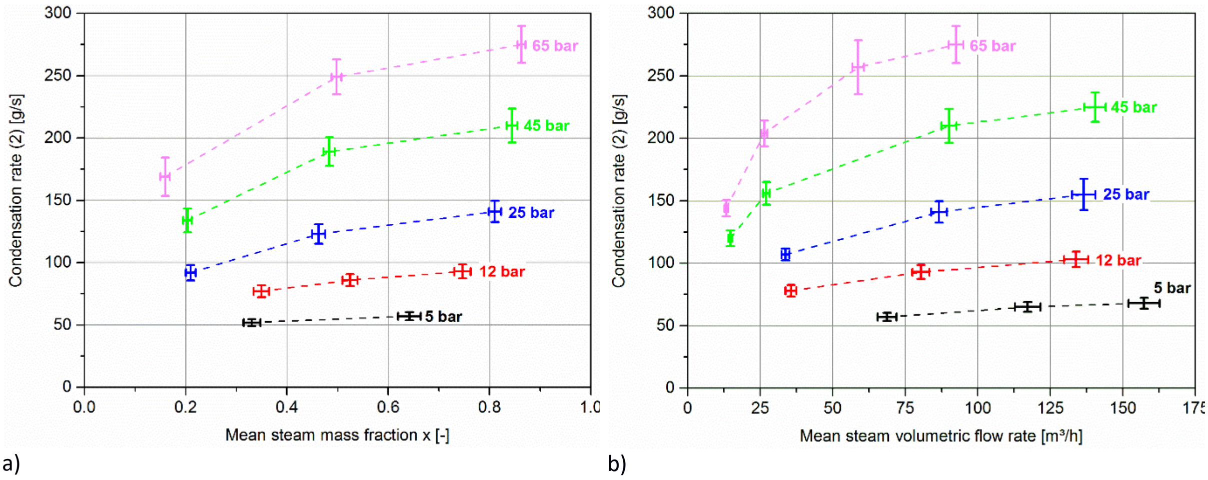

Figure 15: Condensation rates as a function of inlet steam fraction (a) and mean steam volumetric flow rate (b).

4.3 Flow morphology

Eventually, a selection of reconstructed condensate fraction distributions is shown in Table 5. A summary of all results and data processing procedures can be found in Bieberle et al. (2019) [41], [42].

Table 5: Compilation of reconstructed cross-sectional water-steam distributions within the condenser tube at different pressures and inlet flow rates for saturated steam and water injections.

Test #	**Cross-sections** 0  1 condensate fraction .				
	"A"	"B"	"C"	"D"	"E"
s51	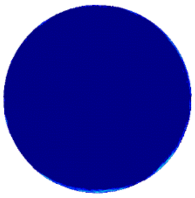	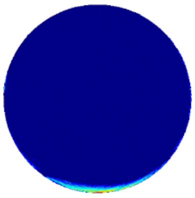	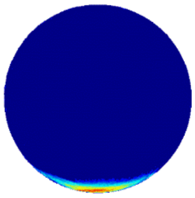	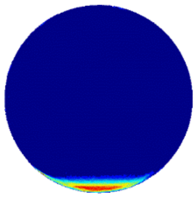	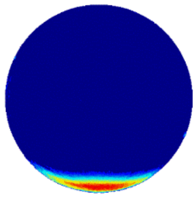
s52	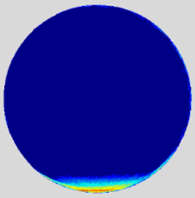	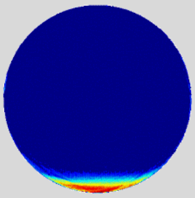	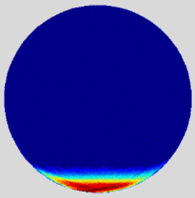	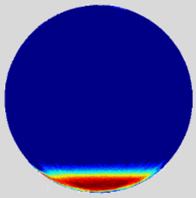	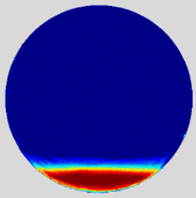
S51a	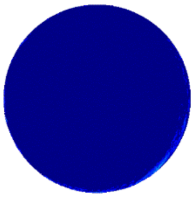	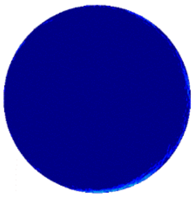	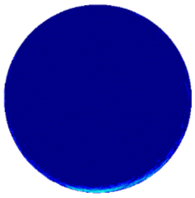	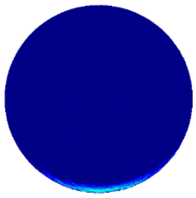	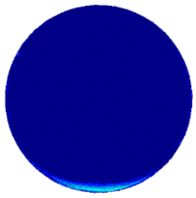
s121	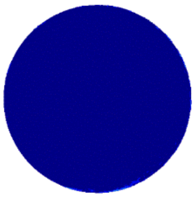	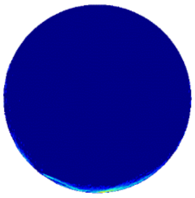	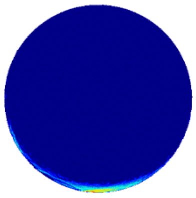	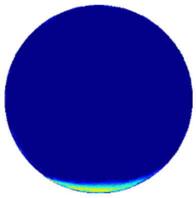	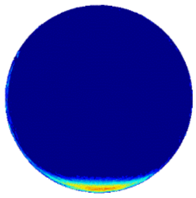
s122	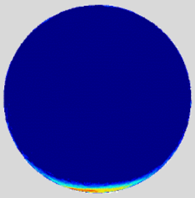	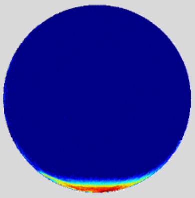	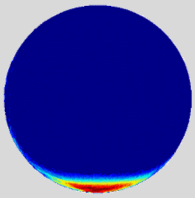	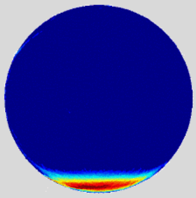	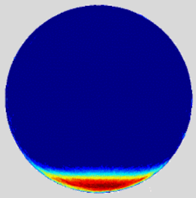
s123	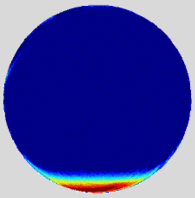	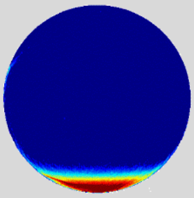	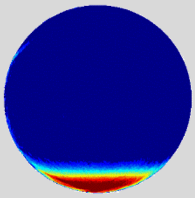	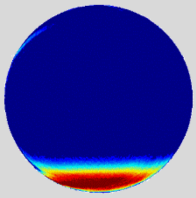	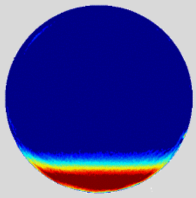
121a	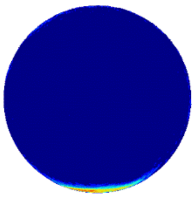	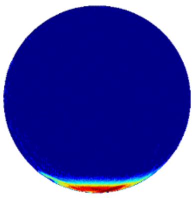	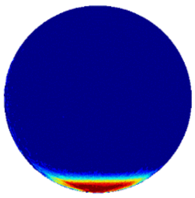	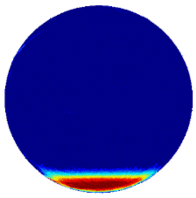	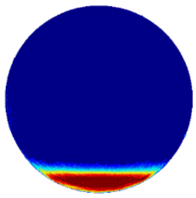

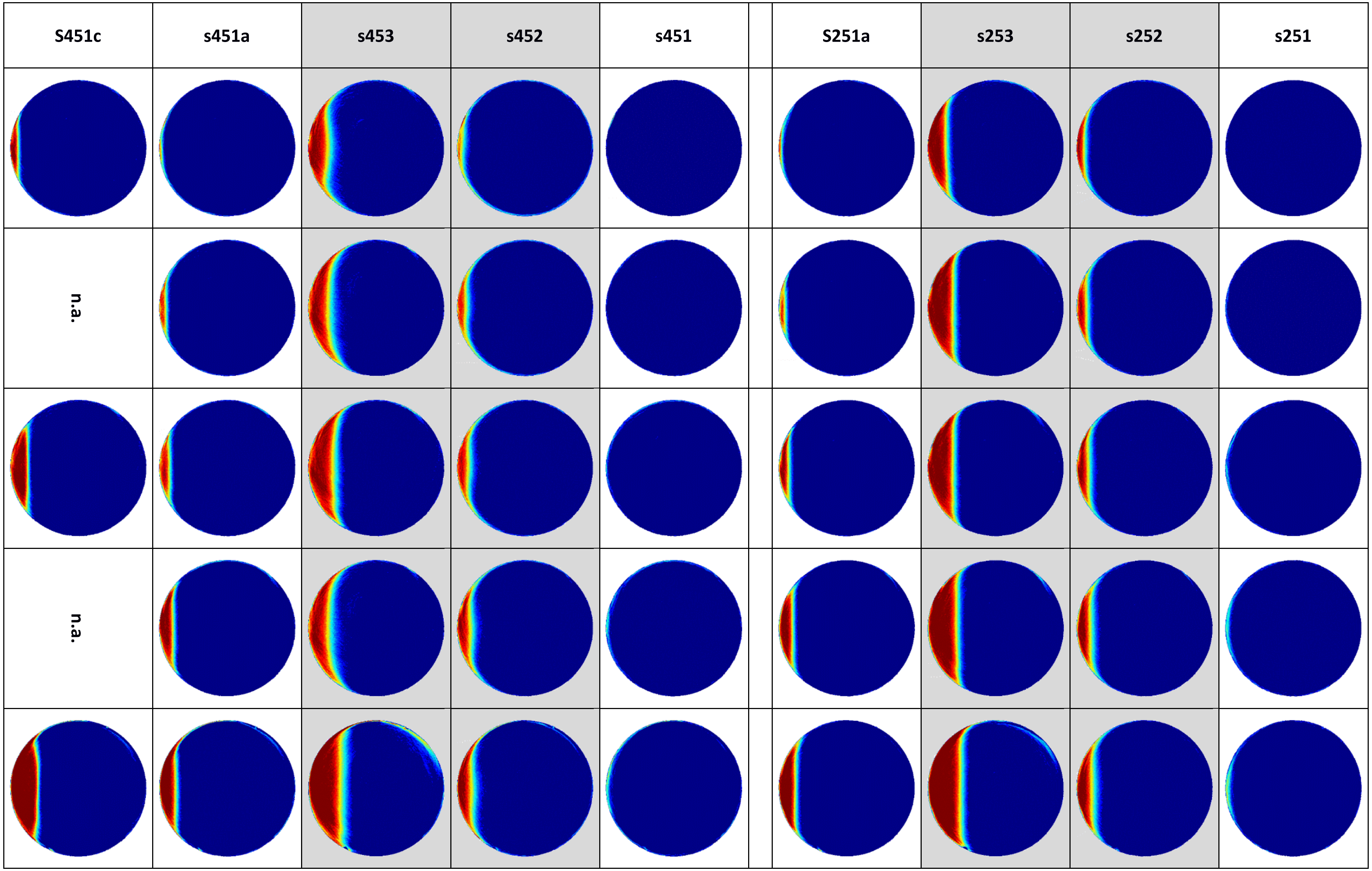
S451c
s451a
s453
s452
s451
S251a
s253
s252
s251
n.a.
n.a.

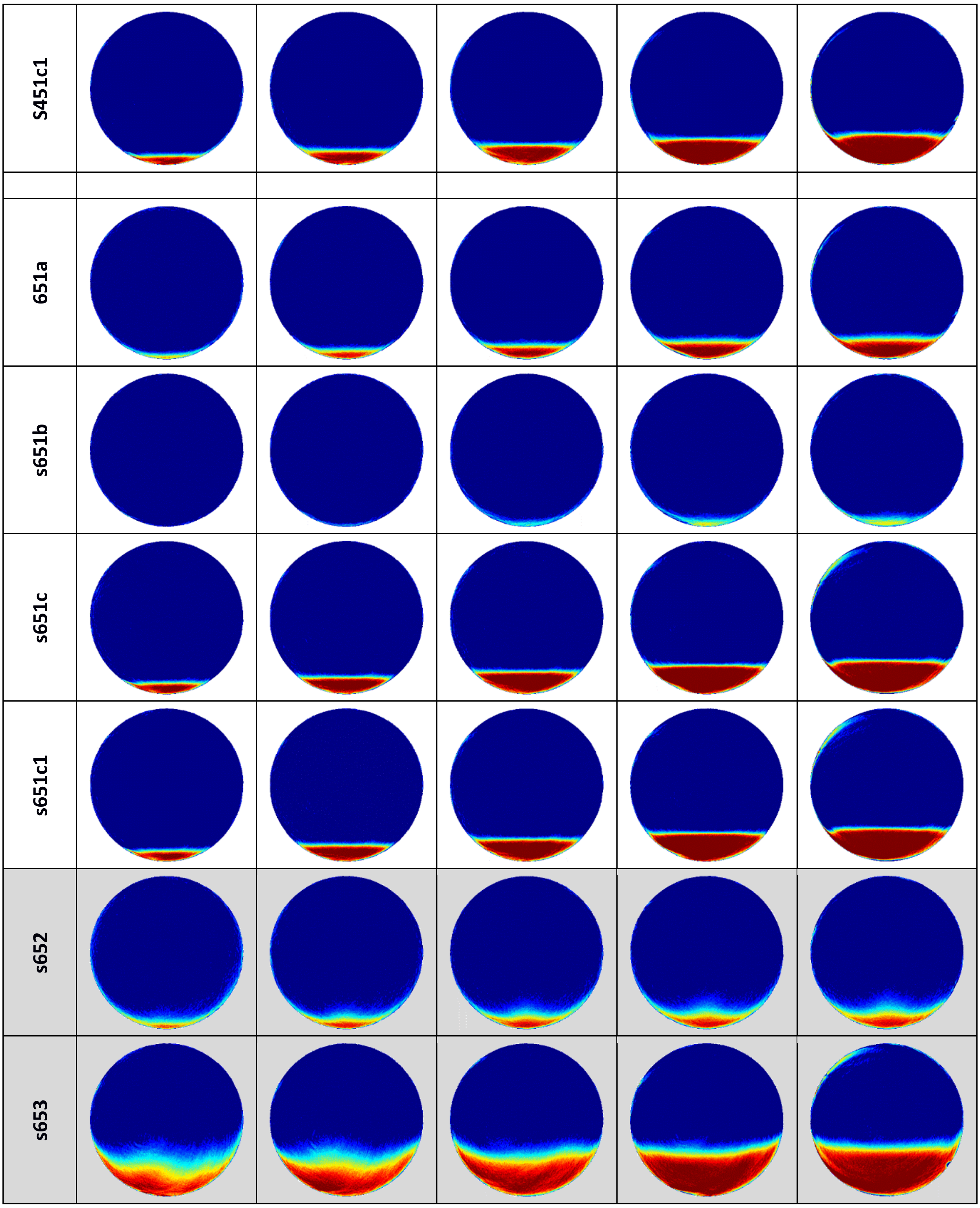

From the obtained condensate/liquid fraction distributions, the stratified condensate levels and their corresponding transition zone were calculated. As an example the condensation level evolution along the condenser tube is shown for 45 bar (Figure 16a) and 65 bar (Figure 16b) each for two different inlet mass flow mixtures. As can be seen, the stratified condensate height follows a linear trend along the condenser tube length.

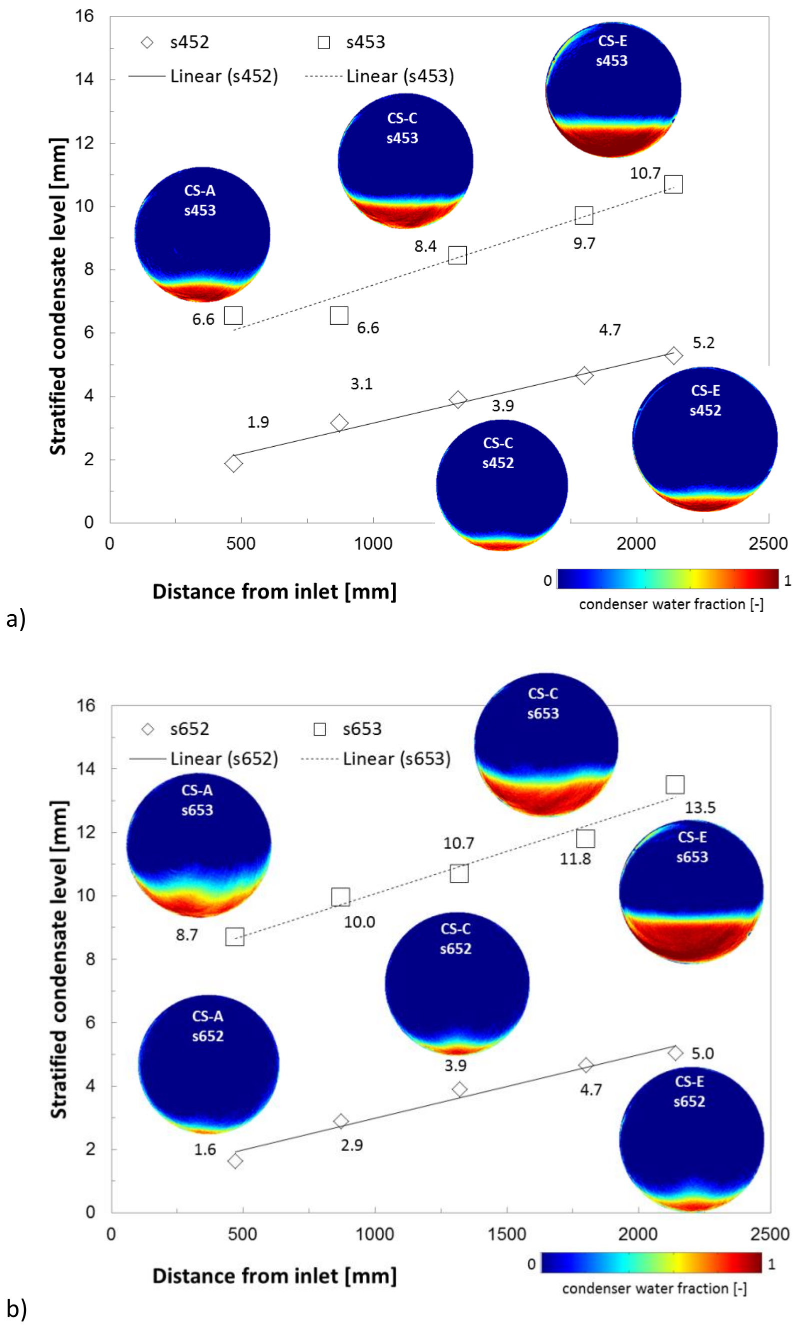

Figure 16: Determined stratified condensate level L_c in the condenser tube at a) 45 bar and b) 65 bar. ("CS" – cross-section).

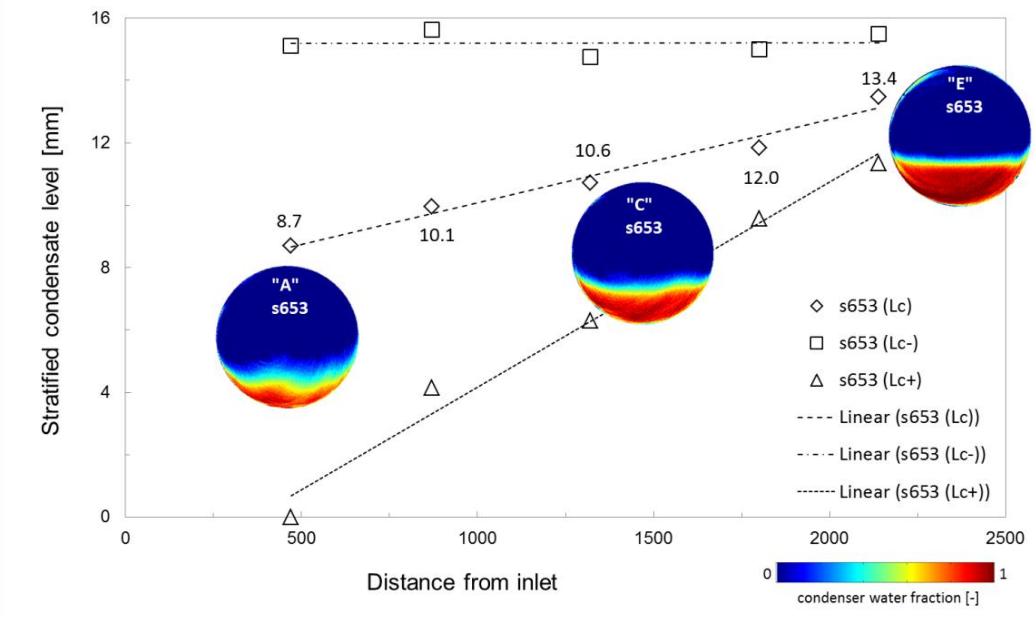

Figure 17: Stratified condensate level L_{c} in the condenser tube at 65 bar (s653) with transition zone (L_{c}^{-} and L_{c}^{+}) indicators.

Besides, Figure 16b and Table 5 reveal in most cases a reduction of the steam-liquid interface thickness with the length of the condenser tube which reflects the expected physics, i.e. along the condenser tube the steam volume flow is reduced and so it is its agitating action on the stratified condensate surface. A detailed analysis is shown in Figure 17 for a measurement at 65 bar. All quantitatively investigated values of L_{c} , L_{c}^{-} and L_{c}^{+} are listed in Table 6.

Eventually, the total steam fraction from the stratified condensate level (SCL) method (Eq. (22)) are compared with the values directly obtained from the reconstructions (Eq. (20) and Eq. (21)) for each cross-section “A”-“E”. As shown in the parity plot in Figure 18a, their deviation is less than 5% which means a good cross-validation for the obtained experimental data. Moreover, the mean total steam fraction (“A”-“E”) of both approaches from the CT scans are compared with the mean total steam fraction taken from the three COSMEA facility approaches, as both represent the integral value of the entire test section. The parity plot in Figure 18b shows again a deviation of about 5%.

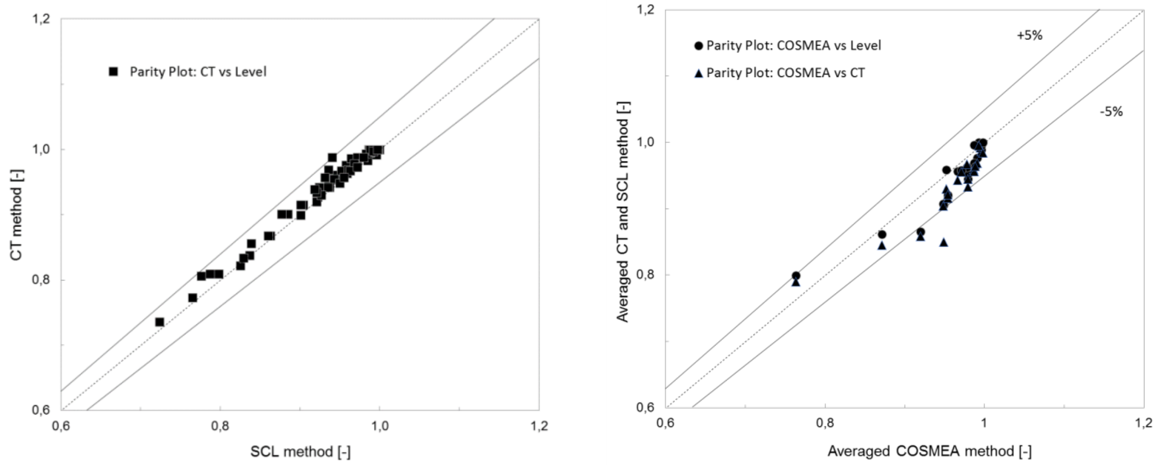

a) b)

Figure 18: Parity plot of the a) mean steam fraction obtained from SCL (stratified condensate level) and CT method and b) averaged mean steam fraction values obtained from the SCL and the CT method versus averaged COSMEA method.

Table 6: Measured total steam fractions from CT scans $\bar{\varepsilon}_{\mathrm{CT}}$ [-] and stratified condensate levels $\bar{\varepsilon}_{\mathrm{L}}$ [-] as well as determined condensate levels $L_{\mathrm{c}}^{(,-,+)}$ [mm] as determined from the CT images at cross-sections “A”–“E”.

Test #	Cross-section: A					Cross-section: B					Cross-section: C					Cross-section: D					Cross-section: E				
	$\bar{\varepsilon}_{\mathrm{CT}}$	$\bar{\varepsilon}_{\mathrm{L}}$	L_c	L_c^-	L_c^+	$\bar{\varepsilon}_{\mathrm{CT}}$	$\bar{\varepsilon}_{\mathrm{L}}$	L_c	L_c^-	L_c^+	$\bar{\varepsilon}_{\mathrm{CT}}$	$\bar{\varepsilon}_{\mathrm{L}}$	L_c	L_c^-	L_c^+	$\bar{\varepsilon}_{\mathrm{CT}}$	$\bar{\varepsilon}_{\mathrm{L}}$	L_c	L_c^-	L_c^+	$\bar{\varepsilon}_{\mathrm{CT}}$	$\bar{\varepsilon}_{\mathrm{L}}$	L_c	L_c^-	L_c^+
s51	1.000	1.000	x	0.6	x	0.991	1.000	x	1.6	x	0.985	0.992	1.3	2.6	x	0.985	0.983	2.0	3.5	x	0.972	0.973	2.8	4.5	1.3
s52	0.996	0.990	1.4	3.4	x	0.972	0.980	2.3	4.3	x	0.960	0.969	3.0	5.4	1.6	0.950	0.948	4.3	6.2	2.9	0.921	0.920	5.8	7.6	4.5
s51a	0.986	1.000	x	x	x	0.981	1.000	x	0.5	x	0.981	1.000	x	1.3	x	0.986	1.000	x	1.6	x	0.987	1.000	x	2.0	x
s121	0.997	1.000	x	x	x	0.986	1.000	x	1.3	x	0.988	0.996	0.8	2.0	x	0.983	0.992	1.3	2.4	x	0.980	0.985	1.9	3.5	x
s122	0.988	0.995	0.9	2.0	x	0.972	0.988	1.6	3.1	x	0.968	0.978	2.4	4.2	1.1	0.963	0.967	3.1	4.9	1.6	0.955	0.955	3.9	5.8	2.1
s123	0.959	0.975	2.6	4.7	1.3	0.946	0.961	3.5	5.7	2.1	0.936	0.948	4.3	6.8	2.8	0.922	0.927	5.4	7.7	3.7	0.901	0.915	6.0	9.1	4.4
s121a	0.978	0.996	0.8	1.8	x	0.962	0.985	1.9	3.7	1.1	0.956	0.971	2.9	4.4	1.9	0.950	0.955	3.9	5.3	2.8	0.936	0.937	4.9	6.4	4.0
s251	0.998	1.000	x	x	x	0.998	1.000	x	x	x	0.987	1.000	x	1.1	x	0.988	1.000	x	1.6	x	0.992	0.998	0.5	2.1	x
s252	0.958	0.975	2.6	4.3	1.1	0.959	0.963	3.4	5.2	1.8	0.944	0.953	4.0	6.2	2.4	0.937	0.942	4.7	6.9	2.9	0.927	0.927	5.4	7.9	3.4
s253	0.904	0.915	6.0	7.9	4.4	0.901	0.899	6.8	8.9	5.2	0.863	0.868	8.2	10.1	6.6	0.837	0.841	9.3	11.2	7.7	0.787	0.809	10.6	12.6	8.8
s251a	0.993	0.996	0.8	1.6	x	0.989	0.983	2.0	3.1	x	0.965	0.967	3.1	4.5	2.3	0.945	0.946	4.4	5.7	3.4	0.928	0.927	5.4	6.6	4.4
s451	0.998	1.000	x	x	x	0.997	1.000	x	x	x	0.993	1.000	x	0.5	x	0.992	1.000	x	1.1	x	0.997	1.000	x	1.4	x
s452	0.964	0.985	1.9	3.9	x	0.952	0.967	3.1	5.5	x	0.943	0.955	3.9	6.6	1.9	0.935	0.942	4.7	7.4	2.5	0.921	0.932	5.2	8.1	2.8
s453	0.885	0.904	6.6	10.1	4.2	0.877	0.904	6.6	10.0	3.8	0.860	0.862	8.4	11.1	5.7	0.829	0.831	9.7	12.2	7.7	0.776	0.806	10.7	13.4	8.4
s451a	0.996	0.996	0.8	1.4	x	0.982	0.981	2.1	3.3	x	0.972	0.965	3.3	4.4	2.0	0.953	0.944	4.5	5.8	3.4	0.933	0.927	5.4	6.8	4.2
s451c	0.967	0.976	2.5	3.5	1.6	x	x	x	x	x	0.923	0.925	5.5	6.6	4.8	x	x	x	x	x	0.858	0.856	8.7	9.6	8.1
s451c1	0.972	0.976	2.5	3.5	1.6	0.950	0.955	3.9	4.9	3.1	0.931	0.925	5.5	6.4	4.8	0.888	0.888	7.3	8.1	6.6	0.865	0.856	8.7	9.4	7.9
s652	0.940	0.988	1.6	5.3	x	0.936	0.971	2.9	6.7	1.1	0.931	0.955	3.9	8.2	1.5	0.924	0.942	4.7	9.2	1.8	0.918	0.934	5.0	11.1	1.9
s653	0.839	0.856	8.7	15.1	x	0.825	0.825	10.0	15.6	4.2	0.798	0.806	10.7	14.7	6.3	0.765	0.777	11.8	15.0	9.6	0.724	0.732	13.5	15.5	11.3
s651a	0.978	0.995	0.9	2.1	x	0.975	0.978	2.4	3.8	1.4	0.959	0.957	3.8	5.3	2.5	0.940	0.937	4.9	6.8	3.7	0.925	0.922	5.7	7.4	4.3
s651b	0.993	1.000	x	x	x	0.995	1.000	x	0.8	x	0.986	1.000	x	2.0	x	0.981	0.993	1.1	3.7	x	0.985	0.989	1.5	4.2	x
s651c	0.956	0.969	3.0	3.9	2.3	0.934	0.942	4.7	5.5	4.0	0.906	0.909	6.3	7.2	5.7	0.864	0.870	8.1	8.7	7.4	0.836	0.841	9.3	10.0	8.7
s651c1	0.961	0.969	3.0	3.9	2.1	0.941	0.944	4.5	5.4	3.9	0.909	0.912	6.2	7.1	5.5	0.872	0.873	7.9	8.7	7.4	0.838	0.844	9.2	10.0	8.6

4.4 Wall heat flux

Beside the condensation rate, the heat flux through the tube wall is a further important parameter for condensation analysis. For that, we processed the data of the heat flux probe, which gives circumferentially distributed inner and outer wall temperatures at one axial position near the condensation tube outlet (Figure 5). Table 7 summarizes the heat fluxes for all condensation tests (Table 3) together with uncertainties.

For further analysis, we included the flume Reynolds number

$$Re_r = \frac{u_{\mathrm{plo}} \cdot d_{\mathrm{hy}}}{\nu} \tag{25}$$

in the table. Here, d_{hy} denotes the hydraulic diameter and ν the kinematic viscosity of the liquid. The mean velocity of the liquid in the flume is

$$u_{\mathrm{plo}} = \frac{\dot{m}_{\mathrm{pli}} + \dot{m}_{\mathrm{c}}}{\rho_{\mathrm{plo}} \cdot A_{\mathrm{r}}}, \tag{26}$$

with the cross-sectional flume area A_{r} (see Eq. (22)). The hydraulic diameter is

$$d_{\mathrm{hy}} = 4 \cdot \frac{A_{\mathrm{r}}}{b}. \tag{27}$$

with b denoting the wetted perimeter, i.e. the total length of peripheral liquid-wall contact.

Table 7: Heat flux along the tube circumference as determined from the heat flux probe data. The second and the third columns give calculated liquid outlet velocities and Reynolds numbers for experimental points where the flume could be reconstructed with sufficient confidence, that is, with a height of $L > 1.5$ mm.

Test #	u_{plo} [m/s]	Re_r	$\dot{q}_{\mathrm{w}} \pm \Delta\dot{q}_{\mathrm{w}}$ [kW/m²]				
			180° (top)	135°	90°	45°	0° (bottom)
s51	1.55	53174	444.4 ±40.4	430.0 ±39.7	413.4 ±37.6	417.7 ±38.6	357.3 ±33.0
s51a			465.3 ±42.3	435.1 ±40.2	430.4 ±39.1	445.6 ±41.1	441.6 ±40.8
s51b			470.4 ±42.7	440.4 ±40.7	437.9 ±39.8	460.6 ±42.5	462.8 ±42.7
s52	0.86	56633	438.4 ±39.9	416.4 ±38.5	409.1 ±37.2	364.2 ±33.7	327.8 ±30.3
s121	4.67	138357	640.8 ±58.2	598.6 ±55.3	591.5 ±53.7	609.7 ±56.3	585.5 ±54.1
s121a	0.97	66643	603.0 ±54.7	573.3 ±52.9	563.5 ±51.2	543.0 ±50.1	467.8 ±43.2
s121b			660.3 ±59.9	617.2 ±57.0	614.4 ±55.8	654.7 ±60.4	648.9 ±59.9
s122	2.27	131324	627.6 ±56.9	589.4 ±54.4	576.6 ±52.3	584.9 ±54.0	539.3 ±49.8
s123	1.45	120657	607.3 ±55.2	580.2 ±53.6	566.4 ±51.5	541.1 ±50.0	495.5 ±45.7
s251			847.8 ±76.9	796.1 ±73.4	786.4 ±71.4	834.6 ±77.0	815.2 ±75.2
s251a	1.21	105188	798.4 ±72.5	748.4 ±69.0	732.6 ±66.5	713.3 ±65.7	621.5 ±57.4
s251b			869.5 ±78.9	829.5 ±76.6	819.8 ±74.4	878.9 ±81.1	865.8 ±79.9
s252	2.95	269560	829.5 ±75.3	775.0 ±71.5	764.0 ±69.3	780.2 ±72.0	732.8 ±67.6

s253	1.46	230284	788.7 ±71.6	750.4 ±69.2	731.0 ±66.4	632.2 ±58.3	648.3 ±59.9
s451			1081.2 ±98.1	1038.0 ±95.7	1024.0 ±92.9	1086.6 ±100.2	1065.2 ±98.3
s451a	1.87	183305	1010.5 ±91.7	936.9 ±86.5	924.3 ±93.9	907.5 ±83.7	816.0 ±75.3
s451b			1097.3 ±99.6	1070.1 ±98.7	1049.0 ±95.2	1130.1 ±104.3	1107.5 ±102.1
s451c	0.72	103294	948.0 ±86.0	879.1 ±81.1	881.5 ±80.0	618.2 ±57.1	602.2 ±55.6
s451c1	0.73	104605	950.0 ±86.2	880.1 ±81.2	882.2 ±80.1	630.1 ±58.1	614.3 ±56.7
s452	5.60	551656	1066.6 ±96.8	1003.4 ±92.5	996.1 ±90.3	1036.0 ±95.5	987.3 ±91.1
s453	2.70	492255	1015.3 ±92.1	940.6 ±86.8	921.9 ±83.7	897.1 ±82.8	899.4 ±83.0
s651			1249.1 ±113.3	1218.3 ±112.3	1193.5 ±108.3	1274.7 ±117.5	1250.1 ±115.3
s651a	2.38	260990	1176.7 ±106.8	1090.4 ±100.6	1080.6 ±98.1	1074.0 ±99.0	989.0 ±91.18
s651b			1228.4 ±111.5	1176.8 ±108.6	1162.9 ±105.5	1219.3 ±112.4	1175.4 ±108.4
s651c	0.83	131147	1095.9 ±99.5	1015.0 ±93.7	1005.2 ±91.2	722.8 ±66.7	651.8 ±60.2
s651c1	0.84	132107	1096.3 ±99.5	1014.9 ±93.6	1004.9 ±91.2	736.7 ±67.9	660.2 ±60.9
s652	8.85	889174	1233.2 ±111.9	1181.4 ±109.0	1172.1 ±106.4	1221.5 ±112.6	1169.1 ±107.8
s653	3.14	740063	1173.8 ±106.5	1085.3 ±100.1	1075.4 ±97.6	1099.3 ±101.4	1086.2 ±100.2

To give an overview about the variation of heat flux regarding to the operational parameters the five circumferential heat flux values per test are averaged using weighting factors which account for assumed symmetry of the flow. Thus, top (180°) and bottom (0°) values are weighted with 1/8 while the other values are double-weighted with 1/4. These averaged heat fluxes are shown in Figure 19 as a function of the outlet steam mass fraction x_{pso} and subject to the outlet steam volumetric flow rate $\dot{V}_{\mathrm{pso}}$ respectively. Other than the condensation rate we relate the heat fluxes to outlet parameters since the local measurement position was near the tube outlet. Similar to the condensation rates also in these plots the influence of the system pressure is clearly visible. The higher the pressure the higher the heat fluxes due to the increasing temperature difference between the inner and outer tube wall. Furthermore, with a higher amount of liquid in the tube the heat flux decreases too. Eventually, a decreasing steam volumetric flow causes a decreasing averaged heat flux due to a significant reduction of the heat transfer coefficient at the inner tube wall.

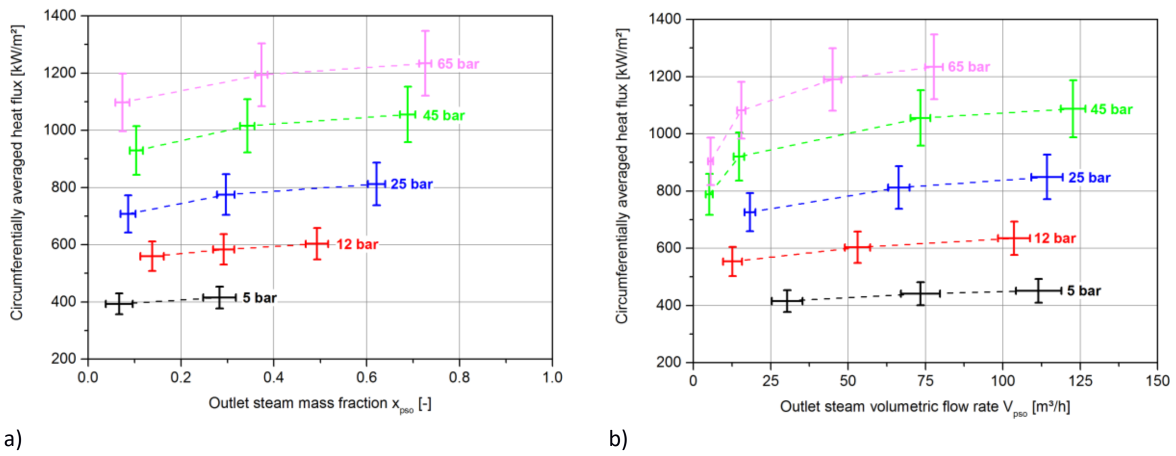

Figure 19: Circumferentially averaged wall heat flux as function (a) of the outlet steam mass fraction and (b) of the outlet steam volumetric flow.

As a representative example the circumferential heat flux distributions of the tests at highest outlet steam flow are shown in Figure 20. Due to the high condensation rates a condensate flume forms at the bottom of the tube. According to the common opinion the heat flux through the flume should be significantly lower than in regions of film condensation. However, we can see an almost equal value along the circumference. At the bottom position (0°), where definitely a liquid flume exists, the heat flux is similar to or even higher than in the top position. In addition, the high values at 45° are remarkable. A plausible explanation is the high steam velocity in the tube (e.g. j_{pso}) that agitates the liquid in the flume by strong interfacial shear. The resulting turbulence in the liquid then promotes heat transfer between the steam-liquid interface and the tube wall.

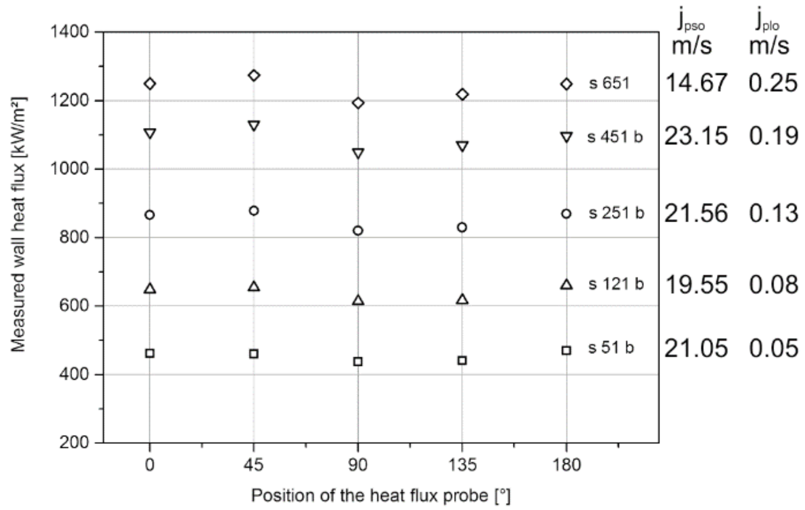

Figure 20: Circumferential wall heat flux at five positions; tests at the highest outlet steam flow and pressures 5-65 bar.

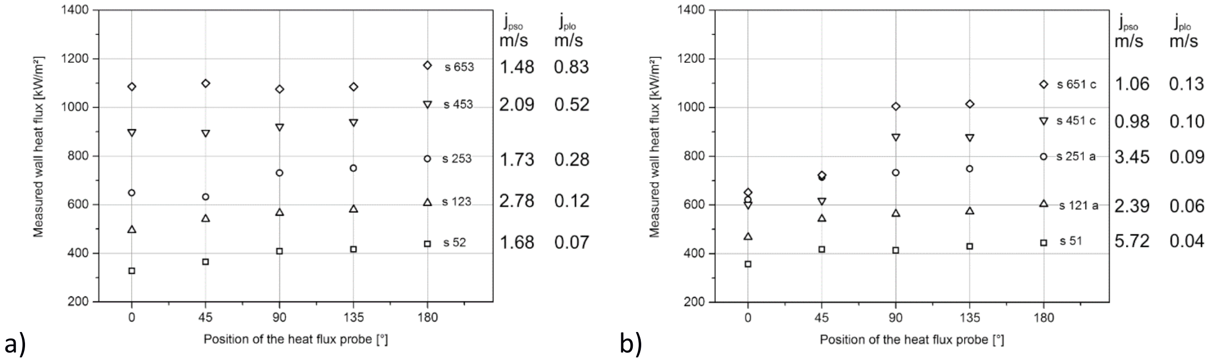

Figure 21: Circumferential wall heat flux a) at high liquid and low steam outlet superficial velocities and b) at low liquid and steam outlet superficial velocities.

The comparison in Figure 21 gives a further indication of this. Figure 21a depicts the tests with the highest amount of liquid injection and Figure 21b tests at the same pressure levels but without liquid flow at the tube inlet. That is, the outlet liquid flow is much higher for tests in Figure 21a as the condensation rate is similar. For the 45 bar and 65 bar tests the heat flux is almost equal at all angles at high outlet liquid velocity (tests s653 and s453) while it is considerably lower in positions 0° and 45° at low outlet liquid velocity (tests s651c and s451c). The Reynolds numbers in Table 7 indicate, that the flume flow is never laminar ($2500 \leq Re_{r,\mathrm{crit}} \leq 4000$). There are three thermal hydraulic effects that can explain this behavior. 1) At higher Reynolds numbers the turbulent heat transfer within the liquid intensifies in such a way that the circumferential heat flux is equalized. Such an explanation is in-line with e.g. surface renewal theory [47], where the surface renewal rate is related to turbulence intensity. 2) With higher interfacial shear interfacial waves build up towards a slug flow which lead to increased heat transfer. According to the flow map of Tandon (Figure 23), case s651c starts as pure steam and ends up in a stratified flow. On the other hand, case s653 starts as annular flow and ends on the boundary of transition region to slug flow. A similar trend is observed for cases s451c and s453. This observation has consistency with the CT data. The CT profiles of these two experiments at cross section E reveal that case s651c is fully stratified with a low interface thickness while case s653 shows a broader and hence wavier interface (Figure 22). Thus, interfacial waves (case s453 and s653) may contribute to a homogenization of the circumferential heat flux by intermittent wall rewetting.

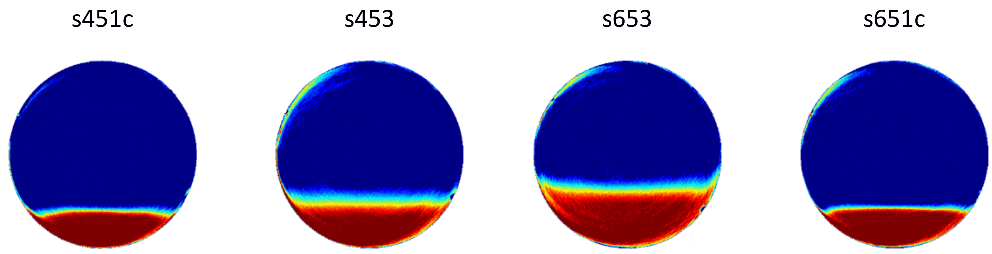

Figure 22: CT profiles at cross-section "E" for 45 bar and 65 bar experiments.

3) The different outlet liquid velocities (listed in Table 7) lead to different residence times of the condensate in the cooled tube. Longer residence times then may lead to a stronger sub-cooling at 0° and 45°. A deeper insight can only be gained by denser instrumentation, higher time resolution of e.g. X-ray tomography or validated CFD simulations.

4.5 Flow classification

The observed flow patterns were compared with theoretical correlations for condensation in horizontal tubes using the established flow map of Tandon et al. [37]. For clarity, steady-state tests are divided in two groups: measurements at low pressure of 5, 12 and 25 bar (see Figure 23, left) and measurements at high pressure of 45 bar and 65 bar (see Figure 23, right). To compare all performed measurements the dimensionless superficial steam velocity

$$j_s^* = \frac{j_s}{\sqrt{g \cdot d_i}} \sqrt{\frac{\rho_s}{\rho_l - \rho_s}}, \qquad \textbf{(28)}$$

as introduced by Wallis & Dobson [38] is plotted against the ratio of the volumetric liquid and steam fraction. Thereby, j_s is the superficial steam velocity, g the gravitational acceleration, ρ_s and ρ_l the steam and liquid density respectively and d_i the inner tube diameter. Using these parameters gives an almost linear classification of the flow regimes in the logarithmic plot.

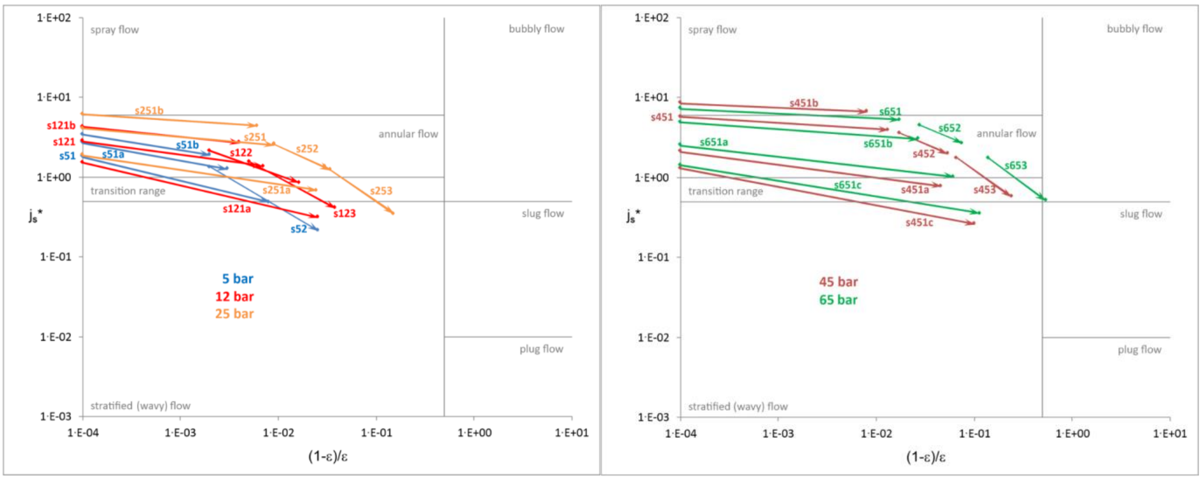

Figure 23: Steady-state condensation experiments within the horizontal flow map of Tandon et al. [37].

Each experimental point is plotted as an arrow with the starting point (left) that corresponds to the inlet conditions and an end point (right) that relates to the outlet conditions. As tests with an initial void fraction of 1 (pure steam) cannot be fit into the logarithmical scale we started the abscissa at 10^{-4}.

The outlet conditions have been calculated from the inlet condition and the condensation rate calculated by the 2nd approach.

Figure 23 shows that most of the tests fall into the annular and transition flow regime, which is due to operational limits of the COSMEA test rig. As we control the pressure by steam feed, as described above, even at low steam mass flow rates we have annular or transition flow due to the high density ratio of liquid and gas, even at 65 bar pressure. Future experiments will be run with a facility modification allows also regimes with low steam fraction. However, as the largest contribution to total condensation is at high steam quality, these experiments are a good basis for heat transfer analyses. Nonetheless, some tests were found to end in stratified flow with a high liquid level as it was confirmed by the X-ray CT water level determination. Examples for that are the tests s52, s121a, s253, s451c and s653.

5. Conclusions

In this paper, the thermal hydraulic test facility COSMEA was introduced that allows single effect studies for high-pressure steam condensation in an inclined tube at up to 65 bar pressure and saturation conditions, i.e. 281 °C. Boundary conditions are given by adjustable steam and water feed rates and a forced convective secondary cooling with water in counter-current flow. We performed experiments in steady-state conditions at pressures of 5, 12, 25, 45 and 65 bar and varying inlet steam qualities. The wall heat flux was measured at five circumferential positions in a given axial position using a custom-made heat flux probe. The averaged cross-sectional flow morphology was non-intrusively investigated by proprietary X-ray CT system at a spatial resolution of approx. 0.5 mm. None of the operating scenarios revealed detectable condensate films, meaning, that their thickness must be less than 0.5 mm. The data has been used for validation of CFD models and simulations, which is subject of the second part of this paper.

Acknowledgment

This work was funded by the German Federal Ministry of Economic Affairs and Energy (BMBF) with the grant number 02NUK041B on the basis of a decision by the German Bundestag. The responsibility for the content of this publication lies with the authors.

REFERENCES

[1] T.L. Schulz, Westinghouse AP1000 advanced passive plant, Nuclear Engineering and Design 236 (2006) 1547-1557.

[2] Stosic, Z.V., Brettschuh, W., Stoll, U., 2008. Boiling water reactor with innovative safety concept: The Generation III+ SWR-1000. Nucl. Eng. Des. 238, 1863–1901. doi:10.1016/j.nucengdes.2007.12.014

[3] Sato, T., Akinaga, M., Kojima, Y., Two types of a passive safety containment for a near future BWR with active and passive safety systems, Nuclear Engineering and Design 239 (2009) 1682–1692

[4] Paladino, D., Dreier, J., Passive containment cooling system (PCCS) response with Drywell Gas Recirculation System (DGRS) activated during a postulated Loss of Coolant Accident (LOCA), Nuclear Engineering and Design 241 (2011) 3925– 3934

[5] Yan, W., Preliminary Study for the Passive Containment Cooling System Analysis of the Advanced PWR, Energy Procedia 39 (2013) 240 – 247

[6] Ha, H., Lee, S., Kim, H., Optimal design of passive containment cooling system for innovative PWR, Nuclear Engineering and Technology 49 (2017) 941e952

[7] Lee, S.W., Heo, S., Ha, H.U., Kim, H.G., The concept of the innovative power reactor, Nuclear Engineering and Technology 49 (2017) 1431e1441

[8] Status Report 82 – KERENA™, IAEA 2011.

[9] Leyer, S., Wich, M., 2012. The Integral Test Facility Karlstein. Sci. Technol. Nucl. Install. 2012, 1–12. doi:10.1155/2012/439374

[10] APEX-AP1000 confirmatory testing to support AP1000 design certification, U.S. Nuclear Regulatory Research Washington, DC 20555-0001

[11] S. Leyer, F.Maisberger, V.Herbst, M.Doll, M. Wich, T. Wagner, Status of the full scale component testing of the KERENA emergency condenser and containment cooling condenser, Proceeding of the International Conference on Advances in Nuclear Power Plants (ICAPP 10), P.5, San Diego, 2010.

[12] T. Wagner, M.Wich, M.Doll, V.Herbst, S.Uhrig, Tests with the emergence condenser at the integral test stand Karlstein for KERENA, Proceedings of the Annual Meeting of Nuclear Technology, Berlin 2010

[13] Wagner, T., Wich, M., Doll, M., Leyer, S., 2011. Full Scale Tests with the Passive Core Flooding System and the Emergency Condenser at the Integral Test Stand Karlstein for KERENA, in: Proceedings of ICAPP'12. Presented at the ICAPP 2011, Nice.

[14] Drescher R., Wagner T., Leyer S. Passive BWR integral LOCA testing at the Karlstein test facility INKA, VGB Power Tech, pp. 33-37, 2014.

[15] Cloppenborg, T., Schuster, C., Hurtado, A., 2015. Two-phase flow phenomena along an adiabatic riser – An experimental study at the test-facility GENEVA, Int. J. of Multiphase Flow 72. 112–132.

[16] Viereckl F., Schuster C., Lippmann W., Hurtado A. Experimental and theoretical investigation of boiling in the slightly inclined tubes of the containment cooling condenser, 49th AMNT, Berlin, 2018.

[17] Prasser, H.-M.; Bottger; A.; Zschau, J.: „A new electrode-mesh tomograph for gas–liquid flows", FlowMeas. Instrum. 9(2), 111–119, 1998

[18] E. F. Hicken, A. Schaffrath, M.Fethke, H.Jaegers , Der NOKO Vesrsuchstand der Forschungszentrum Jülich (FZR) GmbH-Rückblick auf 7 Jahre experimentalle Untersuchungen zur Erhöhung der Sicherheit von Leichtwasserreaktoren, Atomwirtschaft Atomtechnik 47 (2002) 343-348.

[19] Schaffrath, A., 1997. KONWAR - eine Erweiterung von ATHLET zur Berechnung der Kondensation in waagerechten Rohren (No. 3343), Berichte des Forschungszentrums Jülich. Forschungszentrums Jülich, Jülich

[20] Prasser, H.-M., Beyer, M., Carl, H., Manera, A., Pietruske, H., Schütz, P., Weiß, F.-P., 2006. The multipurpose thermalhydraulic test facility TOPFLOW : an overview on experimental capabilities, instrumentation and results. Kerntechnik 163–173

[21] Schaffrath, A.; Krüssenberg, A.-K.; Weiß, F.-P.; Hicken, E.-F.; Beyer, M.; Carl, H.; Prasser, H.-M.; Schuster, J.; Schütz, P.; Tamme, M. (2001). TOPFLOW - a new multipurpose thermalhydraulic test facility for the investigation of steady state and transient two phase flow phenomena. Kerntechnik 66 pp. 209-212

[22] Hampel, U.; Seidel, T.; Beyer, M.; Szalinski, L.; Lucas, D. (2016) Pressure-tank technology for steam-water two-phase flow experiments at elevated pressure and temperature. Specialist Workshop on Advanced Instrumentation and Measurement Techniques for Nuclear Reactor Thermal Hydraulics (SWINTH), Livorno, Italy

[23] E. Krepper, M. Beyer, Experimental and numerical investigations of natural circulation phenomena in passive safety systems for decay heat removal in large pools, Nuclear Engineering and Design 240 (2010) 3170–3177

[24] E. Krepper, Modeling, simulation and experiments on boiling process in pressurized water reactors, Kerntechnic 78(2013) 35-37

[25] E. Krepper, D.Lucas, R.Rzehak, CFD modeling of downward two phase pipe flow, 9th ICMF, 2016, Firenze, Italy

[26] E. Krepper, D.Lucas, T. Frank, M.Prasser, P. Zwart, The inhomogenous MUSIG model for the simulation of polidispersed flows, Nuclear Engineering and Design 238(2008) 1690-1702.

[27] N.Merigoux, P. Apanasevich, J.P. Mehlhoop, D. Lucas, C.Raynaud, A. Badillo, CFD codes benchmark on TOPFLOW-PTS experiment, Nuclear Engineering and Design 321(2017) 288-300.

[28] P.Coste, N.Merigoux, Two-phase CFD validation:TOPFLOW-PTS steady state steam-water tests 3-16, 3-17, 3-18 and 3-19, Nuclear Engineering and Desgin 299 (2016) 18-27

[29] P.Apanasevich, D.Lucas, M.Beyer, L.Szalinski, CFD based approach for modeling direct contact condensation heat transfer in two-phase turbulent stratified flows. International Journal of Thermal Sciences 95(2015) 123-135.

[30] M. Goldbrunner, J. Karl und D. Hein, „Experimental Investigation of Heat Transfer Phenomena During Direct Contact Condensation in the Presence of Noncondensable gas by means of Linear Raman Spectroscopy," in 10th Int. Symp. on Laser Techniques Applied to FluidMechanics, Lisbon, 2000.

[31] A. Hundhausen, H. Müller, S. Kelm, E. Reinecke und H. Allelein, „Towards CFD-Grade measurments in a condensing boundary layer-first measurments of the new SETCOM facility," in the 8th european review meeting on severe accident research, Warsaw, Poland, 2017.

[32] Huggenberger, M., Aubert, C., Bandurski, T., Dreier, J., Fischer, O., Strassberger, H.J., & Yadigaroglu, G. (1999). ESBWR related passive decay heat removal tests in PANDA. ICONE-7: Proceedings of the 7th international conference on nuclear engineering, (p. 4252). Japan: Japan Society of Mechanical Engineers

[33] Kuran, S.; Xu, Y.; Sun, X.; Cheng, L.; Yoon, H. J.; Revankar, S. T.; Ishii, M.; Wang, W. , Startup transient simulation for natural circulation boiling water reactors in PUMA facility, Nuclear Engineering and Design (2006) 2365-2375.

[34] A. Böttger, T. Gocht, H-M. Prasser, and J. Zschau. Transiente Kondensationversuche an einem Notkondensator / Einzelrohr (INVEP) . Technical Report ISSN 1437-322X,Forschungzentrum Rossendorf, 2003.

[35] Seok Kim , Byoung-Uhn Bae, Yun-Je Cho , Yu-Sun Park , Kyoung-Ho Kang , Byong-Jo Yun; An experimental study on the validation of cooling capability for the Passive Auxiliary Feedwater System (PAFS) condensation heat exchanger , Nuclear Engineering and Design 260 (2013) 54–63

[36] Yeon-Sik Kim, Ki-Yong Choi, Hyeon-Sik Park, Seok Cho, Bok-Deug Kim, Nam-Hyeon Choi, Won-Pil Baek; Commissioning of the ATLAS thermal-hydraulic integral test facility ; Annals of Nuclear Energy 35 (2008) 1791–1799

[37] Tandon, T.N., Varma, H.K. and Gupta, C.P. (1982). A new flow regime map for condensation inside horizontal tubes, ASME Journal of Heat Transfer, Vol. 104, pp. 763-768

[38] Wallis, G. B. & Dobson, J. E. (1973). The onset of slugging in horizontal stratified air-water flow. International Journal of Multiphase Flow 1, pp. 173-193

[39] VDI-Wärmeatlas, 10. Auflage. Springer-Verlag Berlin Heidelberg, 2006

[40] Schubert, M.; Bieberle, A.; Barthel, F.; Boden, S.; Hampel, U. (2011) Advanced tomographic techniques for flow imaging in columns with flow distribution packings, Chemie Ingenieur Technik 83/7, pp. 979-991

[41] Bieberle, A., Boden, S., Beyer, M. and Hampel, U. 2018 Results of the stationary measurements at COSMEA-I facility - CT part (https://doi.org/10.14278/rodare.3)

[42] Bieberle, A., Beyer, M., Pietruske, H., Hampel, U., Boden, S. (2019). Investigations on stationary measurements at COSMEA-I facility - CT part. (http://doi.org/10.14278/rodare.127)

[43] ATLAS facility description report, KAERI /TR-3754/2009.

[44] Advanced boiling water reactor (ABWR), Hitachi-GE Nuclear Energy, Ltd (http://www.hitachi-hgne.co.jp/en/download/abwr.pdf)

[45] Birvalski, M., Tummers, M., Delfos, R., & Henkes, R. (2015). Laminar–turbulent transition and wave–turbulence interaction in stratified horizontal two-phase pipe flow. *Journal of Fluid Mechanics, 780*, 439-456. doi:10.1017/jfm.2015.483

[46] Higbie, R. (1935) The rate of absorption of pure gas into a still liquid during a short time of exposure, Transaction of the American Institute of Chemical Engineers, 365-389, 31.

[47] M. Birvalski, M. J. Tummers, R. Delfos and R. A. W. M. Henkes; Laminar–turbulent transition and wave–turbulence interaction in stratified horizontal two-phase pipe flow ;Journal of Fluid Mechancis (2015).